Atmospheric
Measurement
Techniques
Open Access
Discussions

EGU

1 # The CU Mobile Solar Occultation Flux instrument: structure

2 functions and emission rates of NH_3, NO_2 and C_2H_6

3

4 **Natalie Kille[1,2], Sunil Baidar[2,3,a], Philip Handley[2,3,a], Ivan Ortega[2,3,b], Roman**

5 **Sinreich[3], Owen R. Cooper,[4] Frank Hase[5], James W. Hannigan[6], Gabriele Pfister[6],**

6 **and Rainer Volkamer[1,2,3]**

7 [1]{Department of Atmospheric and Oceanic Sciences (ATOC), University of Colorado, Boulder,

8 CO, USA}

9 [2]{Cooperative Institute for Research in Environmental Sciences (CIRES), University of

10 Colorado, Boulder, CO, USA}

11 [3]{Department of Chemistry and Biochemistry, University of Colorado, Boulder, CO, USA}

12 [4]{National Ocean Atmosphere Administration (NOAA), Chemical Sciences Division (CSD),

13 Boulder, CO, USA}

14 [5]{Institut für Meteorologie und Klimaforschung – Atmosphärische Spurengase und

15 Fernerkundung (IMK-ASF), Karlsruhe Institute of Technology (KIT), Karlsruhe, Germany}

16 [6]{National Center for Atmospheric Research (NCAR), Atmospheric Chemistry Observations &

17 Modeling Laboratory (ACOM), Boulder, CO, USA}

18 [a]{now at: NOAA/CSD, Boulder, CO, USA}

19 [b]{now at: NCAR/ACOM, Boulder, CO, USA}

20 Correspondence to: R. Volkamer (rainer.volkamer@colorado.edu)

21

22 **Abstract**

23 We describe the University of Colorado mobile Solar Occultation Flux instrument (CU mobile

24 SOF). The instrument consists of a digital mobile solar tracker that is coupled to a Fourier

25 Transform Spectrometer (FTS, 0.5 cm^{-1} resolution), and a UV-Visible Spectrometer (UV-Vis,

26   0.55 nm resolution). The instrument is used to simultaneously measure the absorption of

27   ammonia (NH_3), ethane (C_2H_6), and nitrogen dioxide (NO_2) along the direct solar beam from a

28   moving laboratory. These direct sun observations provide high photon flux and enable

29   measurements of vertical column densities (VCDs) with geometric air mass factors, high

30   temporal (2 sec) and spatial (5-19 m) resolution. It is shown that the instrument line shape (ILS)

31   of the FTS is independent of the azimuth and elevation angle pointing of the solar tracker.

32   Further, collocated measurements next to a high resolution FTS at the National Center for

33   Atmospheric Research (HR-NCAR-FTS) show that the CU mobile SOF measurements of NH_3

34   and C_2H_6 are precise and accurate; the VCD error at high signal to noise is 2-7 %. During the

35   Front Range Air Pollution and Photochemistry Experiment (FRAPPE, 21 July - 3 September

36   2014) in Colorado, the CU mobile SOF instrument measured median (maximum, minimum)

37   VCDs of 4.3 (45, 0.5) x 10^{16} molecules/cm^2 NH_3, 0.30 (2.23, 0.06) x 10^{16} molecules/cm^2 NO_2,

38   and 3.5 (7.7, 1.5) x 10^{16} molecules/cm^2 C_2H_6. All gases were detected in larger 95 % of the

39   spectra recorded in urban, semi-polluted rural and remote rural areas of the Colorado Front

40   Range. We calculate structure functions based on VCDs, which describe the variability of a gas

41   column over distance, and find the largest variability for NH_3. The structure functions suggest

42   that currently available satellites resolve about 10 % of the observed NH_3 and NO_2 VCD

43   variability in the study area. We further quantify the trace gas emission fluxes of NH_3 and C_2H_6

44   and production rates of NO_2 from concentrated animal feeding operations (CAFO) using the mass

45   balance method, i.e., the closed-loop vector integral of the VCD times wind speed along the drive

46   track. Excellent reproducibility is found for NH_3 fluxes, and to a lesser extent also NO_2

47   production rates on two consecutive days; for C_2H_6 the fluxes are affected by variable upwind

48   conditions. Average emission factors were 12.0 and 11.4 gNH_3/hr/head at 30 °C for feedlots with

49   a combined capacity for ~54,000 cattle, and a dairy farm of ~7400 cattle; the pooled rate of 11.8

50   ± 2.0 gNH_3/hr/head is compatible with the upper range of literature values. At this emission rate

51   the NH_3 source from cattle in Weld County, CO (535,766 cattle) could be underestimated by a

52   factor of 2–10. CAFO soils are found to be a significant source of NO_x. The NO_x source accounts

53   for ~1.2% of the N-flux in NH_3, and has the potential to add ~10% to the overall NO_x emissions

54   in Weld County, and double the NO_x source in remote areas. This potential of CAFO to influence

55   ambient NO_x concentrations on the regional scale is relevant because O_3 formation is NO_x

Atmospheric
Measurement
Techniques
Discussions

Open Access

EGU

56   sensitive in the Colorado Front Range. Emissions of NH_3 and NO_x are relevant for the

57   photochemical O_3 and secondary aerosol formation.

58   **1   Introduction**

59   Gases emitted from anthropogenic sources can have a profound impact on local air quality (Raga

60   et al., 2001, Ramanathan and Feng, 2009) and climate (Stocker et al., 2013). Emissions from

61   large cattle feedlots contain ammonia (NH_3) (Hutchinson et al., 1982, Flesch et al., 2007) which

62   is a precursor for aerosol via the formation of ammonium salts (Walker et al., 2004). NH_3 is a

63   major source for reactive nitrogen to form particulate matter 2.5 (PM2.5), which negatively

64   affects human health (Todd et al., 2008). Ammonium salts form when NH_3 reacts with inorganic

65   (Doyle et al., 1979) and organic (Zhang et al., 2004) acids (Fangmeier et al., 1993). Ammonium

66   is mainly present in the submicron fraction of aerosol and contributes significantly to PM2.5

67   mass worldwide (Zhang et al., 2007). Aerosol can travel a long distance in the atmosphere before

68   deposition, thus affecting greater regions than the local environment (Hristov et al., 2011). Oil

69   and natural gas (ONG) production is a source for fugitive emissions of ethane (C_2H_6) (Xiao et al.,

70   2008), a small volatile alkane, and volatile organic carbon (VOC) precursor of ozone (O_3)

71   (Parrish and Fehsenfeld, 2000). The emissions of C_2H_6 from the ONG sector in areas of hydraulic

72   fracturing are highly uncertain and are an area of active research with interest in emission rates,

73   air quality, and climate impacts (Ahmadov et al., 2015). C_2H_6 contributes to oxidation production

74   of formaldehyde (HCHO) and acetaldehyde (Lou et al., 2007), which is a carcinogen, and

75   precursor for radicals that lead to photochemical O_3 production (Lei et al., 2009, Baidar et al.,

76   2013). HCHO as a radical source also affects the oxidative capacity that is relevant for secondary

77   aerosol formation (Fried et al., 1997, Franco et al., 2015). Nitrogen dioxide (NO_2), emitted during

78   combustion, is a precursor for the formation of photochemical O_3 (Finlayson-Pitts and Pitts Jr.,

79   2000). Only ~10 % of NO_x (=NO+NO_2) emissions from vehicles is in the form of NO_2 directly

80   (Carslaw and Beevers, 2005). Another source of NO_x are soils from feedlots (Denmead et al.,

81   2008). Based on SCIAMACHY satellite observations, Australia and the Sahara produce NO_x

82   predominantly from soil, whereas the United States predominantly produces NO_x from

83   anthropogenic sources, such as combustion (Jaeglé et al., 2005; Bertram et al., 2005). Health

84   effects of O_3 and aerosols require assessment of emissions of the precursor gases. The US

85   Environmental Protection Agency (EPA) recently updated its guidelines for fenceline monitoring

86   to better protect communities near refineries (Jones, 2015).

87   The Solar Occultation Flux (SOF) method uses direct sunlight to determine vertically integrated

88   concentrations of trace gases (Mellqvist et al. 2010). Column observations integrate over the

89   planetary boundary layer height (PBLH) and hence are independent of its changing height.

90   Column measurements can be used to quantify the emission flux/production rate from an area

91   source by driving around the source, or driving upwind and downwind of that source area. The

92   SOF method is complementary to other techniques used to quantify emissions, such as in-situ

93   measurements, or stationary deployment of several commercial EM27/SUN Fourier Transform

94   Spectrometer (FTS) around an area source (Hase et al., 2015, Chen et al., 2016). In-situ

95   measurements, or open-path eddy covariance studies (Baum et al., 2008), provide more localized

96   information, and require access to the site of interest. Micrometerorological gradient methods

97   require assumptions of homogeneity (Todd et al., 2008). One benefit of mobile SOF

98   measurements is that the total amount is quantified remotely, and no assumptions about

99   homogeneity need to be made. With the mobile SOF a source can be isolated, and quantified

100   remotely. The emission flux and source strength is determined by the mass balance approach

101   (Mellqvist et al., 2010; Ibrahim et al., 2010, Baidar et al., 2013).

102   Structure functions (Follette-Cook et al., 2015) characterize how the variability in vertical column

103   densities (VCDs) changes over distance (see section 2.6 and 3.5). We use the structure function to

104   characterize the NH_3, NO_2 and C_2H_6 VCD variability on the spatial scale of a satellite ground

105   pixel. Satellites used to retrieve these gases are for example: the Tropospheric Emission

106   Spectrometer (TES, 5.3 x 8.5 km^2) and Infrared Atmospheric Sounding Interferometer (IASI, 12

107   x 25 km^2) for NH_3 (Van Damme et al., 2014; Dammers et al., 2016; Shephard et al., 2011),

108   Atmospheric Chemistry Experiment – Fourier Transform Infrared Spectrometer (ACE-FTS) and

109   Michelson Interferometer for Passive Atmospheric Sounding (MIPAS) for C_2H_6 (Fischer et al.,

110   2008; Glatthor et al., 2009; Rinsland et al., 2005), SCIAMACHY (15 x 26 km^2) and Ozone

111   Monitoring Instrument (OMI, 13 x 24 km^2) (NO_2) (Boersma et al., 2009). With their large spatial

112   coverage and continuous global monitoring, satellites have the potential to increase knowledge

113   about the large distribution and cycles of gases. However, satellite observations remain not very

114   well validated (Dammers et al., 2016). To our knowledge there currently is no attempt to

115   characterize the sub-satellite ground pixel variability of VCDs for NH_3, NO_2 and C_2H_6.

116

117   **2   Experimental**

118   The University of Colorado (CU) digital mobile solar tracker (Baidar et al., 2016), with an

119   integrated motion compensation system and imaging feedback loop, operates autonomously, and

120   tracks the sun at high precision. Here, this tracker was coupled to a moderate resolution FTS

121   optimized for fast measurements of moderate resolution spectra in the mid-infrared (mid-IR)

122   spectral range. The CU mobile SOF instrument components are shown in Fig. 1 and further

123   specified in Table 1. Figure 1 shows the photons along the direct solar beam are reflected by a set

124   of two mirrors in the solar tracker. A dichroic optic separates the IR from the ultraviolet-visible

125   (UV-Vis) wavelengths, and directs the beam towards the FTS. The UV-Vis wavelengths continue

126   through several optics before entering the optical fiber coupler directing the beam into the UV-

127   Vis grating spectrometer. The FTS has two channels and the UV-Vis spectrometer has one

128   channel (Table 1). The instrumentation was mounted inside a trailer.

129   **2.1   Digital mobile solar tracker**

130   The digital mobile solar tracker has been described in detail elsewhere (Baidar et al. 2016). In

131   brief, it consists of a set of planar mirrors (aluminum); one mirror is mounted directly on the axis

132   of a stepper motor (elevation angle), and one on a rotation stage (azimuth angle). The mirrors are

133   controlled from an embedded computer system (PC104) that is integrated with a motion

134   compensation system to calculate the Euler angles of the sun (coarse tracking), and a real-time

135   imaging feedback loop (fine tracking). During mobile deployment the solar tracker has a

136   demonstrated angular precision of 0.052°, and allows the reliable tracking of the sun even on

137   uneven dirt roads from a moving mobile laboratory. This tracking precision and first trace gas

138   measurements have been demonstrated using the Center-to-Limb darkening (CLD) of solar

139   Fraunhofer lines, and NO_2 at UV-Vis wavelengths. The direct-sun Differential Optical

140   Absorption Spectroscopy (DS-DOAS) NO_2 VCDs have further been compared to NO_2 VCDs

141   measured by MAX-DOAS (Multi Axis DOAS) (Baidar et al., 2016). Here we describe the

142   addition of an FTS to simultaneously measure trace gases at mid-IR wavelengths.

Atmospheric
Measurement
Techniques
Discussions

143   2.2   Mobile SOF EM27 FTS

144   A customized Bruker EM27 FTS was characterized for the use from mobile platforms coupled to

145   the solar tracker (Fig. 1). The EM27 FTS is a Michelson interferometer with a double pendulum

146   design to change the optical path difference (OPD). Our configuration allows for fast scanning

147   (160 kHz) to provide spectra acquisition with 2 Hz time resolution, and includes a zinc selenide

148   (ZnSe) beamsplitter and window, 24V power supply, and a Stirling-cooled sandwich detector,

149   consisting of an indium antimonide (InSb, channel 1) and a mercury cadmium telluride (MCT,

150   channel 2) detector in a single detector housing. Each detector has an active area of 1 mm

151   diameter. The FTS allows for measurements over a wide spectral range in the mid-IR spectral

152   region of the solar spectrum (700 – 5000 cm^{-1}). We did not use an apodization function for the

153   measurements during FRAPPE. Boxcar was selected in order to keep the resolution at its

154   maximum of 0.5 cm^{-1}. Further specifications about the instrument configuration are provided in

155   Table 1.

156   The instrument characterization is described in section 2.4.

157   2.2.1 NH_3 and C_2H_6 retrieval

158   The spectra taken with the MCT detector were corrected for instrument background. An example

159   solar spectrum measured by the MCT and InSb detectors is shown in Fig. 2, where the micro

160   windows used for the C_2H_6 and NH_3 retrieval are highlighted with yellow bars. The MCT spectra

161   were background corrected, and NH_3 VCDs were retrieved using the micro window 950 – 980

162   cm^{-1}. The InSb spectra were used without further corrections for the retrieval of C_2H_6 (2970 -

163   3000 cm^{-1}). The spectral fit windows including interfering species are listed in Table 2. All

164   retrievals were conducted using the SFIT4 software (Hase et al., 2004; Nussbaumer and

165   Hannigan, 2014), and a-priori profile parameters as given in Table 3. SFIT4 uses the vertical

166   profiles of pressure, temperature, and water taken from NCEP (National Centers for

167   Environmental Prediction) and WACCM (Whole Atmosphere Community Climate Model,

168   https://www2.acom.ucar.edu/gcm/waccm) at given altitudes that were assumed to be constant

169   throughout each day. It uses updated C_2H_6 lines from Harrison et al. (2010), and HITRAN 2008

170   (Rothman et al., 2009) line lists for all other absorbers listed in Table 2. The a-priori error allows

171   for the VCD of interest (NH_3 or C_2H_6) to vary by a factor of 100 over the a-priori value (Table 3);

Atmospheric
Measurement
Techniques

Open Access

Discussions

172   the interfering gases (e.g. CO_2 and H_2O) were allowed less variability. SFIT iterates to obtain a

173   best fit between the calculated and measured spectrum. The residual parameter (%rms) is used to

174   quality assure our data. The quality assurance cut-off %rms value has been determined by

175   contrasting $\frac{1}{\sqrt{N}} \cdot Noise$ against the residual, where N is the cumulative number of spectra that

176   have a %rms less than or equal to the threshold, and $Noise$ is the spread of residuals within the

177   threshold. The cut-off %rms has been taken as three times the minimum of the $\frac{1}{\sqrt{N}} \cdot Noise$

178   against the residual plot, and was determined to be 3.6 for NH_3 and 6.4 for C_2H_6. This translates

179   to ~75 % of NH_3 and ~47 % of C_2H_6 spectra were considered during analysis. Spectral proof of

180   the detection of both gases is shown in Fig. 2. In that shown case the detected gas column density

181   of C_2H_6 has a value of 7.13 x 10^{16} molecules/cm^2, and for NH_3 a value of 40.2 x 10^{16}

182   molecules/cm^2 which is well above the detection limit (section 3.1.1). The top panel of the fit

183   window shows the residual between observed and fitted spectrum. Besides the observed and

184   fitted spectrum the fit window also includes the strongest interfering trace gases.

185   **2.3   UV-Vis spectrometer**

186   The UV-Vis channel consists of an OceanOptics QE65000 grating spectrometer to measure NO_2

187   VCDs. The spectrometer has a charge-coupled device detector covering the spectral range 390 –

188   520 nm as is described elsewhere (Baidar et al., 2016).

189   **2.3.1 NO_2 retrieval**

190   NO_2 was measured by the UV-Vis spectrometer using the retrievals described in Baidar et al.

191   (2016). In brief, NO_2 was retrieved in the spectral fitting window 434 – 460 nm using the

192   WinDOAS software (Van Roozendael and Fayt, 2001). Baidar et al. (2016) also have compared

193   the DS-DOAS NO_2 VCDs with MAX-DOAS to assess benefits of high photon fluxes for

194   sensitivity, and validate the NO_2 measurements.

Atmospheric
Measurement
Techniques
Discussions

2.4 Mobile SOF characterization

2.4.1 Comparison at NCAR

Prior to field deployment the mobile laboratory had been collocated at the National Center for Atmospheric Research (NCAR) in Boulder, CO with a high resolution Bruker 120HR FTS (HR-NCAR-FTS). The CU mobile SOF instrument was mounted in a trailer that was parked in the parking lot ~50 m away from the HR-NCAR-FTS, assuring that both instruments observed the nearly same air mass. Coincident time intervals of the measurements were evaluated to determine the accuracy of the trace gas VCDs, and the limit of detection (LOD) of the 0.5 cm^{-1} resolution FTS. We calculate the LOD using the following IUPAC definition (IUPAC, 2006):

$$\text{LOD}_{\text{exp}} = k \cdot \sigma_{\text{Gaussian}} + \left| \text{background} \right|, \tag{1}$$

where k is a factor chosen according to the confidence interval, σ_{Gaussian} is the standard deviation during a time period in which the air mass is not changing (i.e., constant C_2H_6 and NH_3 VCD). We set $k = 3$ for a 99.7 % confidence interval. Here, the LOD is given in units of VCD and determines the minimum amount of a gas to be detected in order to be statistically distinct from a blank measure (Long and Winefordner, 1983, Schrader, 1995). Each morning before a research drive and - if the cloud cover permitted - in the afternoon after a research drive, stationary measurements were taken in a parking lot at CU (40.005 °N, 105.270 °W) to determine σ$_{\text{Gaussian}}$, and were found to be consistent with the σ$_{\text{Gaussian}}$ determined at NCAR shown in Fig. 3. The figure shows the VCD measurements of NH_3 and C_2H_6 from the HR-NCAR-FTS in blue, and mobile SOF data in black. Mobile SOF VCD measurements were taken at specific integration times. A longer integration time averages more scans, and reduces the noise in the data. For the background determination mobile SOF data points within the integration time of one HR-NCAR-FTS were averaged. The background was calculated as the difference between mobile SOF FTS and HR-NCAR-FTS data points. See section 3.1.1 for discussion on the comparison.

2.4.2 Characterization of the ILS

For measurements from the mobile laboratory the azimuth and elevation angles change rapidly over the course of a research drive. It is therefore important to characterize the ILS (Hase et al., 1999) over a wide range of azimuth and elevation angle pairs. This was tested in a laboratory

Atmospheric
Measurement
Techniques
Open Access
Discussions
EGU

223   setup where the solar tracker was pointed at a glowbar to observe atmospheric water vapor over a

224   distance of several meters along the path between the FTS and the glowbar. The light emitted by

225   the glowbar is collimated, and directed onto the solar tracker. The FTS with solar tracker is

226   positioned on a rotatable platform. The ILS has been determined using the retrieval code

227   LINEFIT (Hase et al., 1999) version 14 using water vapor absorption lines in the spectral range at

228   1950 – 1900 cm^{-1} for the InSb and at 1820 – 1800 cm^{-1} for the MCT detector. The modulation

229   efficiency at maximum OPD is shown in Fig. 4 for different azimuthal and elevation angles, and

230   the results are further discussed in section 3.1.2 and Table 4.

231   **2.5   Flux calculations**

232   VCD measurements around a site of interest were used in combination with wind fields to

233   calculate the emission flux using the mass balance approach (Mellqvist et al. 2010; Ibrahim et al.,

234   2010; Baidar et al., 2013). The flux is calculated from the following equation:

235    $\text{Net Flux} = \int_S VCD\, \vec{F} \cdot \vec{n}\, ds$,   (2)

236   where VCD is the vertical column density (molecules/cm^2), $\vec{F}$ is the wind vector (m/s), $\vec{n}$ is the

237   outward facing normal with respect to the driving direction, and the integral over ds (m)

238   represents the drive track around a closed box. In order to determine the emission flux or

239   production rate of a gas the wind vector needs to be known.

240   We use model wind to perform the flux calculations to obtain emission fluxes. The model wind

241   (extracted from the North American Mesoscale Model using the National Emission Inventory

242   2011 version 2 (NAM, NEI 2011v2) and with inner domain of 4 km) was interpolated for hourly

243   instantaneous values at 36 altitudes from ~10-50 m above ground to ~18.5 km along the exact

244   drive track coordinate and time.

245   Prior to using the model wind it was compared to the surface wind speed and direction observed

246   at the recording station in Eaton, CO, which was ~5 – 20 km away from the drive track. The

247   comparison of the surface layer of the model wind and the station wind for RD11 is shown in Fig.

248   S1. The surface wind speeds are generally slower than the lowest model wind speed. In the

249   beginning of the research drive the wind speeds do agree well while the wind direction varies a

250   maximal 180°. On average, the wind direction agrees within 90°. We are comparing the

251 stationary recorded surface wind speed with the model wind speed along our drive track, and it is

252 possible that the recorded wind in Eaton was in fact different than 20 km away on the research

253 drive. Based on the comparison we determine the model wind has an uncertainty of 30 %.

254 The NH_3, NO_2, and C_2H_6 fluxes calculated from our VCD measurements and model wind are

255 shown in section 3.3, and the SI text.

256 **2.6 Structure Function**

257 The structure function to assess the spatial scales of VCD variability is defined as:

258 $$f(Z,y) = \left\langle\ |Z(x+y) - Z(x)|^q\ \right\rangle, \tag{3}$$

259 where $\left\langle\ \right\rangle$ denotes the average difference in VCD within distance y, Z is the VCD of a gas of

260 interest, and q is a scaling exponent (Harris et al., 2001, Follette-Cook et al., 2015). Setting q

261 equal to 1 this structure function is a useful tool to quantify trace gas variability over distance. At

262 small distances between measurements the structure function exhibits the largest rate of change,

263 and increases until converging at larger distances. Variabilities increase as both plumes and

264 background air masses are observed. At a certain spatial distance the structure function converges

265 against a maximum VCD variability. We define the variability length scale to determine over

266 which spatial scales a certain percentage of the maximum median variability is observed. The

267 spatial distance at which the VCD variability is 50 % that value of the maximum variability is

268 denoted as $L_V(50\%)$. Then

269 $$L_v(P) = d(P \cdot V_{max}), \tag{4}$$

270 where L_V denotes the variability length scale [km] for a certain percentage P and $d(P \cdot V_{max})$

271 denotes the distance in kilometers at which the VCD variability equals $P \cdot V_{max}$. Here, V_{max} is the

272 maximum median variability.

273 We plot the structure function with units of distance in kilometers on the abscissa, VCD

274 difference has units of molecules/cm^2 on the ordinate, and a second ordinate scales the VCD

275 difference with respect to the median VCD ($\Delta VCD/VCD_{med}$, [%]).

276

3   Results and Discussion

3.1   Mobile SOF performance

3.1.1   Precision and Accuracy

Figure 3 illustrates the data used to determine the LOD and accuracy of the CU mobile SOF. The absolute values of the difference between the VCDs averaged over identical time intervals measured by the HR-NCAR-FTS and by the mobile SOF were used to quantify accuracy. The results are presented in Table 4. The findings for measurement precision and accuracy (see section 2.4 Eq. 1) result in the following LODs: LOD_{NH3} = 0.10 x 10^{16} molecules/cm^2 and LOD_{C2H6} = 0.13 x 10^{16} molecules/cm^2. The accuracy is composed of uncertainty in the cross section, the error associated with the spectral fit, and the uncertainty on the retrieved VCD due to the ILS effect (see section 3.1.2). With an accuracy of 4.4 % for NH_3 and 6.7 % for C_2H_6 and the above given LOD values this means that the accuracy is limiting the overall uncertainty in trace gas observations at concentrations greater than 2.27 x 10^{16} molecules/cm^2 for NH_3 and 1.94 x 10^{16} molecules/cm^2 for C_2H_6. During FRAPPE, the VCDs were greater than the LOD in 99.98 % (NH_3) and 100 % (C_2H_6) of the measurements, which means the LOD was an issue in a low amount of measurements. In terms of the total error (Table 4) this means that the uncertainty was determined by the accuracy of the observed median and maximum, and the LOD was limiting the uncertainty on the minimum observed VCD. For a median VCD of 4.32 x 10^{16} molecules/cm^2 (NH_3) the uncertainty is 0.19 x 10^{16} molecules/cm^2, and for a median VCD of 3.49 x 10^{16} molecules/cm^2 (C_2H_6) the uncertainty is 0.23 x 10^{16} molecules/cm^2.

3.1.2   Instrument Line Shape

While driving a around a source area or site of interest there are 90° changes in the azimuth angle with each turn, and many smaller degree changes in both elevation and azimuth angles due to fine tracking on uneven dirt roads. Column density measurements along the ~2.0 m long beam between the collimated light source of a glowbar and the spectrometer at solar tracker azimuth angles from 0 – 360° and at elevation angles of 5, 45, and 65° were recorded to determine the ILS based on water vapor lines (section 2.6). Figure 4 shows the modulation efficiency at maximum OPD as a function of azimuth angle. The inner circle shows the measurements for the MCT

Atmospheric
Measurement
Techniques
Discussions

305   detector, the outer circle shows the measurements for the InSb detector. Figure 5 shows both the

306   modulation efficiency and phase error as a function of OPD. The top plots show the InSb results,

307   the bottom plots show the MCT results. It can be seen that the modulation efficiency of both

308   detectors shows rather constant behavior. From these experiments it was determined that the

309   MCT detector has a modulation efficiency of 0.968 at maximum OPD and the InSb detector has a

310   modulation efficiency of 1.010 at maximum OPD. These values are obtained by averaging the

311   modulation efficiency at maximum OPD over all azimuth and elevation angle.

312   To investigate the effect of the ILS on the retrieval of NH_3 and C_2H_6, the retrieval software was

313   first run using an ideal ILS as input, and then using the ILS measured for the MCT and InSb

314   detector respectively and comparing the VCD output with ideal and measured ILS. There was 0.5

315   % change in the retrieved NH_3 VCD and 0.0 % change in the C_2H_6 VCD. These results are listed

316   in Table 4 and are factored into the total error on VCDs. We conclude that there is no significant

317   angular dependency on the ILS.

318   **3.2   Mobile SOF deployment**

319   The drive track for the case study from 13 August 2014 is shown in Fig. 6. The 5 sites indicated

320   in that figure contain feedlots and ONG storage tanks. On 12 and 13 August 2014, RD10 and

321   RD11, respectively, the following median (minimum/maximum) VCDs were observed. NH_3: 4.3

322   (0.5/45), C_2H_6: 3.5 (1.5/7.7), NO_2: 0.4 (0.06/2.2) x 10^{16} molecules/cm^2.

323   The variability in total column densities during RD11 is shown in Fig. 7 and Fig. 8. The identical

324   figures for RD10 are included as Fig. S2 and Fig. S3 in the Supplement. Both research drives

325   show similar features in VCD enhancement (VCD - $VCD_{background}$) of the gases, temperature, and

326   wind. Figure 7 shows the VCD time series of the three gases, a time series for the temperature

327   and PBLH, and the model wind speed and direction. NH_3 shows significant column enhancement

328   for site 2, which was the concentrated animal feeding operation (CAFO) with ~54,000 cattle. NO_2

329   also shows some VCD enhancement for site 2. Figure 8 shows the VCD timeseries in form of a

330   Google Earth visualization to indicate the spatial distribution. Sites 1 and 2 are also shown

331   enlarged to visualize the downwind and upwind effects. Site 1 is a source for both NH_3 and C_2H_6.

332   There is a dairy farm located near the west end of the site, and a source for C_2H_6 in the upper

333   right of the site. The VCD enhancement of NO_2 at the south leg of the site is due to heavy traffic

334   on that street. Site 2 for NH$_3$ shows the column enhancement downwind of the cattle feedlot, and

335   a background VCD upwind of the cattle feedlot. For that same site NO$_2$ shows a larger column

336   enhancement downwind than upwind. C$_2$H$_6$ is mostly transported through site 2, as can be seen in

337   that the VCD is on the same color scale upwind and downwind of site 2.

3.3   Emission fluxes

339   The emission fluxes were calculated according to Eq. 2 described in section 2.5. The wind used

340   for flux calculations has been averaged within the planetary boundary layer (Fig. 7). Figure 8

341   panels c and e show the flux as timeseries for each site. The stretch downwind of a site shows

342   positive flux values if the site is a source. If the site is not a source, and a gas is passing through

343   the site, then the absolute value of negative incoming flux and positive outgoing flux are expected

344   to be comparable.

345   The calculated net fluxes are presented in Table 5 for RD10 and RD11. Particularly we could

346   verify that cattle and dairy farms (sites 1, 2 and 4) are significant sources for NH$_3$, and that the

347   soil in site 2 (CAFO) is a significant source of NO$_x$, which we observed in terms of a positive

348   NO$_2$ production rate. The numbers in Table 5 reflect the uncertainty of the spectroscopic data,

349   and the wind data. The error due to the atmospheric variability is not accounted for explicitly in

350   these error bars. The individual gas fluxes are discussed in the following three subsections.

3.3.1   NH$_3$ fluxes

352   For sites 1, 2, and 4, the dairy and cattle feedlots are a source of NH$_3$ during both research drives.

353   The emission flux in site 2 with the largest head count of cattle shows agreement of better than 10

354   % for RD10 and RD11. The average flux is 649 ± 24 kgNH$_3$/hr for 54,044 cattle. This

355   consistency between two days gives confidence in that the uncertainty in the wind is

356   conservatively estimated here. The average emission factor for site 2 is 12.0 ± 2.8 gNH$_3$/hr/head

357   for both days during daytime in the summer. The uncertainty here combines the day-to-day

358   variability and error in the wind (taken as $30\% / \sqrt{2}$). For the dairy farm in site 4 we obtain 11.4

359   ± 3.5 gNH$_3$/hr/head. The per head emission flux from the two samples at site 2 and one sample at

360   site 4 can be pooled resulting in an average emission factor of 11.8 ± 2.1 gNH$_3$/hr/head. The head

361   count for site 1 was unknown, but can be estimated based on the pooled per head emission. The

Atmospheric
Measurement
Techniques
Discussions

Open Access

362   average emission flux from site 1 of 108 kg/hr corresponds to ~9200 cattle. During RD11 the

363   upwind effect influenced the observed VCD at site 4 and precluded quantification of a flux. This

364   means the upwind flux was significant, and variability during the course of driving around the

365   site may have influenced the observed flux. A comparison of the determined NH_3 fluxes to

366   literature values is given in section 3.4.1.

367   ### 3.3.2 NO_2 production rates

368   Soils are sources of NO_x, which is primarily emitted as NO as a result of microbial activity

369   (Zörner et al., 2016). NO_2 is subsequently produced from the reaction $NO + O_3 \rightarrow NO_2 + O_2$ in

370   the atmosphere. Both research drives consistently showed site 2 is a significant source of NO_x,

371   with an average measured NO_2 production rate of 14.5 kg/hr. The difference in the NO_2 emission

372   flux from 18 kg/hr during RD10 and 11 kg/hr during RD11 may represent differences in wind

373   speed. During RD10 the wind speed was approximately 1 to 2 m/s slower than on RD11 (Fig. 7;

374   Fig. S2), allowing for less time for NO into NO_2 conversion during transport. The reaction rate

375   constant for the above reaction is $k = 3.0 \times 10^{-12} \times e^{-1500/T}$ cm^3/molec/s (Sander et al., 2006),

376   which at a temperature of 300 K corresponds to a value for the rate constant of 2.02×10^{-14}

377   cm^3/molec/s during our case studies. On RD10 and RD11 O_3 concentrations of 68 and 79 ppb

378   (Pierce, 2016) correspond to a NO lifetime of ~35 s (75 ppbv O_3). With wind speeds of ~4 m/s

379   NO was converted into NO_2 over a distance of ~140 m (RD11), and maybe twice this number

380   during RD10. In particular, there is sufficient time to convert most of the NO emissions into NO_2

381   within the CAFO area of 1.6×1.6 km^2. To estimate the NO_2/NO ratio under photostationary

382   state, we also need to consider the photochemical destruction of NO_2 from the reaction $NO_2 + O_2$

383    $\rightarrow$(hv) $NO + O_3$. Assuming a typical photolysis frequency, $J(NO_2)$, as $\sim 8 \times 10^{-3}$ s^{-1}, the NO_2/NO

384   ratio is 3.6, indicating that ~80 % of NO_x is visible as NO_2. The average measured NO_2

385   production rate thus corresponds to a NO_x emission rate of 18.6 ± 7.4 kg/hr for site 2. For a

386   fraction of the nearby soil emission there may not be sufficient time to reach the photochemical

387   steady state, but this fraction is likely small. We conclude that the observed NO_2 is a lower limit

388   for the overall NO_x production. The NO_x flux is compared to the emission inventory (EPA 2015)

389   in section 3.4.2.

390   We are able to determine that the NO_x is coming from the feedlot soil rather than point sources

391   such as diesel generators or trucks. Based on Gaussian Plume Modeling a source point that is a

392   distance of 1.7 km away from the measurement location (greatest distance of downwind

393   measurement to a potential diesel generator for the beef feedlot at site 2) can have dispersed

394   horizontally up to 300 m. We measured NO_2 column enhancement over a distance greater ~1.4

395   km indicating that the source of NO_x is the entire feedlot area.

396   3.3.3 C_2H_6 fluxes

397   C_2H_6 has a relatively long atmospheric lifetime of about two months, and is lost in the reaction

398   with OH (OH + C_2H_6 -> C_2H_5 + H_2O). Assuming an OH concentration of 8×10^6 molecules/cm^3

399   and taking the OH reaction rate constant of 2.4×10^{-13} cm^3/molec/s (Sander et al., 2006), the

400   lifetime of C_2H_6 is 60 days which gives rise to a Northern Hemisphere (NH) background VCD

401   (e.g. 3.1×10^{16} molecules/cm^2 at Kiruna, Sweden; Angelbratt et al., 2011). C_2H_6 VCD

402   enhancements over the NH background are therefore expected to mix on regional scales, and are

403   subject to significant transport in the atmosphere. The research drives measured the lowest VCDs

404   of C_2H_6 in Boulder County, CO with its moratorium on fracking. Enhanced VCDs were observed

405   throughout Weld County, CO in areas with active ONG production. The influence from upwind

406   sources makes the quantification of C_2H_6 emission fluxes a bit more challenging. We consistently

407   were able to quantify a positive emission flux out of site 1, as shown in Table 5. Site 1 was also

408   influenced from upwind sources, but the mean C_2H_6 flux was calculated as 63.5 kg/hr with an

409   uncertainty of 29 kg/hr. The C_2H_6 flux is compared to the emission inventory (EPA 2015) in

410   section 3.4.3.

411   3.4   Comparison with literature values

412   3.4.1 NH_3 fluxes from CAFO

413   We compare the NH_3 per head emission rate from cattle and dairy with literature values in Table

414   6. In section 3.3.1 we calculated the emission rate of NH_3 for cattle to be 11.8 ± 2.1 g/hr/head

415   based on the beef and dairy farm estimated capacity and observed NH_3 VCDs. Notably, it is not

416   guaranteed that during the research drive the feedlot was at maximum occupancy. If the

417   occupancy was lower than the maximum occupancy, the value of 11.8 g/hr/head would be a

418   lower limit of the actual per head emission rate. The area of site 2 is mostly covered by two cattle

419   feedlots, such that the likelihood of measuring NH_3 from another source such as fertilizers is low.

420   The comparison with literature values in Table 6 shows that our per head emission factor of NH_3

421   is near the upper range of reported values, and higher by a factor of 1.1 to 8.9. Plausible

422   explanations may be due to differences in environmental conditions such as air temperature,

423   variations in the food, and operation practices employed at CAFO outside of Colorado. An

424   overview of location and conditions that were tested is given in Table 6. Generally the emission

425   is higher in spring and summer when temperatures are warmer than in winter, when the emission

426   is lower. However, the highest previously reported emission factor of 10.4 g/hr/head was

427   obtained under significantly colder temperatures (Bjorneberg et al., 2009), suggesting that factors

428   other than temperature contribute to the significant variability among literature values.

429   Additionally we compare the NH_3 emission flux with the NEI 2011 emission inventory (EPA

430   2015). The inventory has been formatted to a 3 km WRF-Chem grid, and the emissions for July

431   2011 are given as hourly intervals, and do not distinguish between different source sectors.

432   Agriculture is responsible for the major share of NH_3 emissions in the Colorado Front Range.

433   Figure S4 shows the NEI 2011 emission flux during mid-day, when the NH_3 emissions are

434   largest. We compare the emission flux of NH_3 in several ways. The first approach is to use Weld

435   County, CO where the emission inventory suggests an average NH_3 flux of 0.32 kg/km^2/hr for the

436   maximum daytime emissions during summer. Based on our average per head emission factor, and

437   a maximum head count of 535,766 cattle from beef and dairy feedlots in Weld County, CO in

438   2014 (Daniel Bon, 2016, personal communication), the NH_3 emission flux is 0.63 kg/km^2/hr.

439   That means that the EPA (2011) inventory underestimates the NH_3 emission for the total county

440   by about a factor of 2. Focusing on the area within Weld County, CO containing the 5 sites

441   probed during our RDs, the inventory suggests the NH_3 emission flux is 0.65 kg/km^2/hr compared

442   to the NH_3 flux of 6.39 kg/km^2/hr based on head count within the area. This represents an

443   underestimation by a factor of about 10. The differences with the NEI are estimated

444   conservatively here, and could be lower limits if other NH_3 sources were located within the

445   county, but not captured by our measurements, or if the CAFOs probed were not a maximum

446   capacity. The emission inventory is from a few years prior to the research drives, and the total

447   emission of the feedlots may have increased, as may have the number of feedlots within the grid

Atmospheric
Measurement
Techniques
Discussions

448   cells. The 2007 Census of Agriculture for Weld County, CO indicates 565,327 as number of

449   cattle and calves, the 2012 Census indicates 501,446, and for 2014 the capacity was 535,766.

450   Even if the number of feedlots within individual grid cells changed, the capacity did not change

451   by more than 12 % which does not describe the underestimation of NH_3 emission that we

452   quantified. Finally, more case studies are needed for a firm assessment of the NEI in Colorado,

453   despite the significant sample size of CAFOs, excellent reproducibility among different sites, and

454   on different days that we observe in this study. We conclude that using the NEI 2011 emission

455   inventory in Air Quality models most likely underestimates the actual NH_3 emissions during

456   FRAPPE by a factor of 2-10.

457   **3.4.2 NO_x emissions from CAFO**

458   We have consistently observed significant NO_x emissions from CAFO with a rate of 7.3 ± 2.9

459    $kg/km^2/hr$ from site 2, or 18.6 kg/hr during both RDs. No sharp plumes were observed downwind

460   of the site (see Fig. 7c, 8-2d, and Supplementary Fig. S2c, S3-2d). The NO_2 column

461   enhancements closely resemble the area of cattle feeding operations, which suggests the observed

462   NO_x is emitted from microbial activity in the CAFO soils, rather than a stationary combustion

463   source. In order to assess the potential relevance of the enhanced soil emissions of NO_x from

464   CAFOs for the overall NO_x emissions in Weld County, CO we determine the NO_x production rate

465   for cattle as 0.34 g/hr/head from site 2. Notably, the fact that we did not observe NO_x emissions

466   from other sites is compatible with this assumption. At the feedlot in site 4 we were not able to

467   obtain a reproducible flux on RD10 and RD11; instead, the emission was slightly positive on

468   RD10 and negative on RD11 due to an upwind plume affecting the measurements (Table 5).

469   Using the per head NO_x flux as determined based on site 2, the NO_x flux for site 4 would have

470   been 2.5 kg/hr, compared to the average NO_x flux of 1.7 ± 0.5 kg/hr during RD10. There is thus

471   reasonable agreement if the difference in the CAFO capacity is accounted for. Based on the total

472   count of 533,766 cattle in Weld County, CO and an area of 10,404 km^2 we obtain an average

473   contribution from CAFO soil emissions of 0.018 $kg/km^2/hr$. The inventory produces a NO_x flux

474   of 0.17 $kg/km^2/hr$ averaged over Weld County, CO (EPA 2015), which includes emissions from

475   urban areas. We conclude that the NO_x source associated with enhanced microbial activity in

476   CAFO soils could potentially contribute ~10 % to the overall NO_x emissions of Weld County,

477   CO.

Atmospheric
Measurement
Techniques
Open Access

EGU

Discussions

478   The contribution is even higher in the remote area of the five sites probed during the RDs. Here,

479   the inventory produces an average NO_x flux of 0.15 $kg/km^2/hr$. Based on the total count of

480   224,469 cattle in the CAFOs distributed over the area of 414 km^2 shown in Fig. S4 (bottom panel

481   for NO_2), the NO_x source from CAFO soils corresponds to 0.18 $kg/km^2/hr$. We conclude that the

482   CAFO soil emissions can double the NO_x source in the inventory in the area probed by our case

483   studies.

484   This potentially significant contribution of soil NO_x from CAFO is particularly relevant, because

485   the photochemical O_3 formation in the Colorado Front Range is NO_x limited. Missing sources of

486   NO_x in the NEI directly translate into underestimates in the photochemical O_3 production rate in

487   the Front Range, which is an O_3 Non Attainment Area. Very little quantitative information is

488   currently available on NO_x emissions from CAFO. We did not make any attempts to retrieve NO

489   from the CU mobile SOF spectra, which hold potential to complement the NO_2 VCD

490   observations in the future.

491   **3.4.3 C_2H_6 emissions**

492   We determined that the C_2H_6 emission for site 1 is 63.5 ± 29 kg/hr. The NEI 2011 emission

493   inventory (EPA 2015) estimates the C_2H_6 emission for that area as 2.39 $kg/km^2/hr$. Scaling our

494   emission rate to the area of that one grid cell of the inventory (9 km^2), we obtain ~7 $kg/km^2/hr$

495   from site 1. While these measurements indicate the capability of mobile SOF to quantify elevated

496   fluxes of C_2H_6, possibly from leaks, this flux is likely not representative of the greater area of the

497   county. The CU mobile SOF C_2H_6 measurements obtained on a regional scale are most useful if

498   combined with a regional scale chemistry transport model or inverse model to estimate the C_2H_6

499   emissions in the Colorado Front Range. From in-situ observations the ratio of C_2H_6/CH_4 for ONG

500   emissions in Weld County, CO has been measured as 18.4 % (Alan Fried, personal

501   communication), 11 % (Amy Townsend-Small, personal communication), and 10 % (Terra

502   Yacovitch, personal communication). Based on the average ratio of 13.1 ± 4.6 %, and the

503   emission flux for C_2H_6, the CH_4 emission flux is 39.2 – 82.7 $kg/km^2/hr$ at site 1.

Atmospheric
Measurement
Techniques
Discussions

Open Access

EGU

3.5   Spatial variability

504

505   The structure function for the NH_3, NO_2 and C_2H_6 VCDs are shown in Fig. 9. We applied a time

506   constraint of 30 minutes to calculate the structure functions (see section 2.6 Eq. 3), in order to

507   minimize changes in atmospheric state due to transport. Over the first few bins column

508   differences in plumes are small due to measurements being in close vicinity of each other. At

509   greater distances column differences increase, and converge onto a plateau that is determined by

510   the variability between plumes and background air masses.

511   During RD10 and RD11 we observed the highest spatial variability for NH_3, somewhat lower

512   variability for NO_2, and the smallest variability for C_2H_6 VCDs. The observed plateau values

513   were 2.52×10^{16} molecules/cm^2 for NH_3, 0.13×10^{16} molecules/cm^2 for NO_2, and 0.57×10^{16}

514   molecules/cm^2 for C_2H_6, which correspond to 58.6, 32.5, and 16.3 % of the median VCD for

515   NH_3, NO_2, and C_2H_6, respectively. These plateau values should be viewed as specific for our

516   study area, and may differ significantly for urban areas, where the sources may be more

517   distributed.

518   The precision of our NH_3 and C_2H_6 measurements (Table 4) determines how well we can resolve

519   variability in VCDs. If the VCD difference is smaller than the measurement precision, then the

520   VCD differences may be insignificant within our measurement precision. While the mobile SOF

521   probed VCDs at spatial resolution of 5 – 19 m, we are able to resolve significant variability on

522   spatial scales greater than 25 m for all gases. The variability length scales (see section 2.6, Eq. 4)

523   of NH_3, NO_2 and C_2H_6 for 50 % and 90 % variability as well as the length scale near the LOD are

524   given in Table 7. The 50 % and 90 % variability length scales are similar for all gases despite

525   their different plateau values, with Lv(50%) occurring at distances well below 2 km, and

526   Lv(90%) occurring at distances near and below 6 km.

527   The feedlots in sites 1, 2, and 4 which are sources for NH_3 have a minimum width of 400 m (site

528   1 and 4) and 800 m (site 2). Our results are thus consistent with the expected plume diameters in

529   close vicinity to these sites.

530   The current satellites measuring NH_3 have a horizontal resolution of 5.3 x 8.5 km^2 (TES), and 12

531   x 25 km^2 (IASI). Satellites measuring NO_2 have a horizontal resolution of 13 x 24 km^2 (OMI), 40

532   x 80 km^2 (GOME2), 15 x 26 km^2 (SCIAMACHY). The expected resolution of TEMPO

Atmospheric
Measurement
Techniques
Discussions

533   (Tropospheric Emissions: Monitoring of Pollution) from geostationary orbit is 2 x 4.5 km^2 (to be

534   launched in 2019). We observe significant variability (>90 %) in VCDs at variability length

535   scales smaller than ~6 km for NH$_3$ and C$_2$H$_6$, and ~13 km for NO$_2$ (Table 7). This indicates that

536   satellites are able to quantify 10 % of the total variability in VCDs. Future satellites such as

537   TEMPO and GEMS have a horizontal resolution that will begin to approach the scales over

538   which NO$_2$ VCDs vary by 50 % in the atmosphere, though some averaging from limited grid-size

539   resolution can still be expected.

540

541   **4   Conclusion and Outlook**

542   We describe the CU mobile SOF instrument, characterize it, and demonstrate first applications to

543   characterize structure functions, and quantify emission fluxes of NH$_3$, NO$_x$, and C$_2$H$_6$. The

544   instrument can be extended to measure other trace gases that absorb at UV-Vis-IR wavelengths,

545   i.e., sulfur dioxide (SO$_2$), nitric oxide (NO), nitrous acid (HONO), hydrogen cyanide (HCN),

546   acetylene (C$_2$H$_2$), methanol (CH$_3$OH), formic acid (HCOOH), formaldehyde (HCHO), glyoxal

547   (C$_2$H$_2$O$_2$), ozone (O$_3$), among others. We conclude:

548   •   The FTS is well suited to detect typical VCDs in the Colorado Front Range with excellent

549   signal-to-noise. The NH$_3$, NO$_2$ and C$_2$H$_6$ VCDs were above the instrument detection limit

550   in 99.98 %, 95.89 % and 100 % of the spectra, respectively. The CU mobile SOF

551   instrument line shape is not affected by changes in azimuth or elevation angles, providing

552   robust spectral retrievals also while driving on dirt roads, or around corners.

553   •   The total VCD error is 4.4% for NH$_3$, 6.7% for C$_2$H$_6$, and 5% for NO$_2$ at high signal to

554   noise, and accuracy of 0.10 x 10^{16} molecules/cm^2 for NH$_3$ and 0.13 x 10^{16} molecules/cm^2

555   for C$_2$H$_6$. The error limiting the spectroscopic measurement is the cross section

556   uncertainty. The uncertainty in the flux calculations is limited by the knowledge about the

557   winds, consistent with earlier conclusions (Mellqvist et al., 2010). Determination of the

558   spatial variability and structure function is not limited by the instrument precision, unless

559   at very low distances (<25 m). This is similar to earlier findings for in-situ data (Follette-

560   Cook et al., 2015).

Atmospheric
Measurement
Techniques
Discussions

561 • Significant variability in the VCDs is observed for all gases on scales smaller than 6 km,
562   and found 50 % of the VCD variability was at distances shorter than 2 km. Most of this
563   variability happens on scales smaller than current ground pixel sizes of satellites. At the
564   available spatial resolutions, satellites currently quantify less than 10 % of the observed
565   VCD variability. Future missions from geostationary orbit (i.e., TEMPO, GEMS,
566   Sentinel4) will have smaller ground-pixels, which can resolve 10 to <50 % of the
567   variability observed in the NO_2 VCDs.

568 • Emission fluxes for NH_3 during the summer day time are generally underestimated in the
569   NEI 2011 emission inventory, as well as NO_x emissions from CAFO soil. This indicates
570   there are sources that have not been accounted for in the inventory. We determined that
571   the per head emission of NH_3 during two summer days is underestimated by a factor of 2
572   – 10 than determined by other literature and the emission inventory. Emissions of NO_x
573   from microbiological activity in CAFO soils account for ~10 % of the total NO_x emission
574   in Weld County, CO and can double the NO_x source in the rural agricultural areas studied.

575 The CU mobile SOF instrument provides a versatile, efficient and robust tool to improve the
576 statistics of emission fluxes of NH_3, NO_x, C_2H_6 (no losses in sampling lines), study emissions of
577 other gases, and study variations in emissions with temperature, in different seasons, from point
578 and area sources inside and outside of Colorado. The quality of the emission flux estimates
579 benefits from independent wind measurements, and closer attention to upwind effects in
580 particular for C_2H_6. The airborne deployment of the CU mobile SOF instrument is planned for
581 summer 2016, and holds potential to make mobile SOF measurements independent of roads,
582 which is of interest to the studies in more complex terrain, e.g., of biomass burning events.

583 **List of primary chemicals and acronyms**

584 C_2H_6 – ethane

585 HCHO – formaldehyde

586 NH_3 – ammonia

587 NO_2 – nitrogen dioxide

588 NO_x – sum of nitric oxide (NO) and NO_2

589 CAFO – concentrated animal feeding operation

590 CU – University of Colorado

591   DOAS – Differential Optical Absorption Spectroscopy

592   DS-DOAS – direct-sun DOAS

593   EPA – Environmental Protection Agency

594   FRAPPE – Front Range Air Pollution and Photochemistry Experiment

595   FTS – Fourier Transform Spectrometer

596   HR-NCAR-FTS – high resolution FTS at the National Center for Atmospheric Research

597   ILS – instrument line shape

598   InSb – indium antimonide

599   IR – infrared

600   LOD – limit of detection

601   MAX-DOAS – Multi Axis DOAS

602   MCT – mercury cadmium telluride

603   ONG – oil and natural gas

604   OPD – optical path difference

605   PBLH – planetary boundary layer height

606   SOF – Solar Occultation Flux

607   UV-Vis – Ultraviolet-Visible

608   VCD – vertical column density

609

610   **Author contributions**

611   R.V. designed research; N.K., S.B., I.O., R.S., and R.V. conducted the measurements; P.H. and

612   O.R.C. helped during the field deployment; O.R.C., F.H., J.W.H., and G.P. added tools and

613   expertise during analysis; N.K. and S.B. analyzed the data; N. K. and R.V. prepared the

614   manuscript with contributions from all co-authors.

615

616   **Acknowledgements**

Atmospheric
Measurement
Techniques
Discussions

Open Access

EGU

627

628   **References**

629   Ahmadov, R., McKeen, S., Trainer, M., Banta, R., Brewer, A., Brown, S., Edwards, P. M.,

630   de Gouw, J. A., Frost, G. J., Gilman, J., Helmig, D., Johnson, B., Karion, A., Koss, A.,

631   Langford, A., Lerner, B., Olson, J., Oltmans, S., Peischl, J., Pétron, G., Pichugina, Y.,

632   Roberts, J. M., Ryerson, T., Schnell, R., Senff, C., Sweeney, C., Thompson, C., Veres, P. R.,

633   Warneke, C., Wild, R., Williams, E. J., Yuan, B., and Zamora, R.: Understanding high

634   wintertime ozone pollution events in an oil- and natural gas-producing region of the western

635   US, Atmos. Chem. Phys., 15, 411-429, doi:10.5194/acp-15-411-2015, 2015.

636   Angelbratt, J., et al.: Carbon monoxide (CO) and ethane (C_2H_6) trends from ground-based solar

637   FTIR measurements at six European stations, comparison and sensitivity analysis with the

638   EMEP model, Atmos. Chem. Phys., 11, 9253-9269, doi:10.5194/acp-11-9253-2011, 2011.

639   Baidar, S., Volkamer, R., Alvarez, R., Brewer, A., Davies, F., Langford, A., Oetjen, H., Pearson,

640   G., Senff, C., and Hardesty, R. M.: Combining Active and Passive Airborne Remote Sensing

641   to Quantify NO_2 and O_x Production near Bakersfield, CA, 2013, British Journal for

642   Environmental and Climate Change, 3(4), 566-586, doi:10.9734/BJECC/2013/5740, 2013.

643   Baidar S., Kille, N., Ortega, I., Sinreich, R., Thomson, D., Hannigan, J., and Volkamer, R.:

644   Development of a digital mobile solar tracker, Atmos. Meas. Tech., 9, 963-972,

645   doi:10.5194/amt-9-963-2016, 2016.

646   Baum, K. A., Ham, J. M., Brunsell, N. A., and Coyne, P. I.: Surface boundary layer of cattle

647   feedlots: Implications for air emissions measurement, Agric. For. Meteorol., 148, 1882-1893,

648   doi:10.1016/j.agrformet.2008.06.017, 2008.

Atmospheric
Measurement
Techniques
Discussions

649   Bertram, T. H., Heckel, A., Richter, A., Burrows, J. P., and Cohen, R. C.: Satellite measurements
650   of daily variations in soil NO_x emissions, Geophys. Res. Lett., 32, L24812,
651   doi:10.1029/2005GL024640, 2005.

652   Bjorneberg, D. L., Leytem, A. B., Westermann, D. T., Griffiths, P. R., Shao, L., and Pollard, M.
653   J.: Measurement of Atmospheric Ammonia, Methane, and Nitrous Oxide at a Concentrated
654   Dairy Production Facility in Southern Idaho Using Open-Path FTIR Spectrometry, T.
655   ASABE, 52(5), 1749-1756, doi:10.13031/2013.29137, 2009.

656   Boersma, K. F., Jacob, D. J., Trainic, M., Rudich, Y., DeSmedt, I., Dirksen, R., and Eskes, H. J.:
657   Validation of urban NO2 concentrations and their diurnal and seasonal variations observed
658   from the SCIAMACHY and OMI sensors using in situ surface measurements in Israeli cities,
659   Atmos. Chem. Phys., 9, 3867–3879, 2009.

660   Carslaw, D. C., and Beevers, S. D.: Estimations of road vehicle primary NO2 exhaust emission
661   fractions using monitoring data in London, Atmos. Env., 39(1), 167-177, ISSN 1352-2310,
662   doi:10.1016/j.atmosenv.2004.08.053, 2005.

663   Chen, J., et al.: Differential Column Measurements Using Compact Solar-Tracking
664   Spectrometers, Atmos. Chem. Phys. Discuss., doi:10.5194/acp-2015-1058, 2016.

665   Dammers, E., et al.: An evaluation of IASI-NH_3 with ground-based FTIR measurements, Atmos.
666   Chem. Phys. Discuss., doi:10.5194/acp-2016-141, 2016.

667   Denmead, O. T., Chen, D., Griffith, D. W. T., Loh, Z. M., Bai, M., and Naylor, T: Emissions of
668   the indirect greenhouse gases NH_3 and NO_x from Australian beef cattle feedlots, Aust. J. Exp.
669   Agric., 48, 213-218, 2008.

670   Doyle, G. J., Tuazon, E. C., Graham, R. A., Mischke, T. M., Winer, A. M., and PittsJr., J. N.:
671   Simultaneous concentrations of ammonia and nitric acid in a polluted atmosphere and their
672   equilibrium relationship to particulate ammonium nitrate, Environ. Sci. Technol., 13(11),
673   1416-1419, doi:10.1021/es60159a010, 1979.

674   Environmental Protection Agency (EPA): 2011 National Emission Inventory version 2, 2015.

Atmospheric
Measurement
Techniques
Discussions

675   Fangmeier, A., Hadwiger-Fangmeier, A., Van der Eerden, L., and Jäger, H.-J.: Effects of
676   Atmospheric Ammonia on Vegetation – A Review, Environ. Poll., 86, 43-82,
677   doi:10.1016/0269-7491(94)90008-6, 1994.

678   Finlayson-Pitts, B. J., and Pitts Jr., J. N.: Chemistry of the Upper and Lower Atmosphere,
679   Academic Press, San Diego, CA, 882-886, 2000.

680   Fischer, H., Birk, M., Blom, C., Carli, B., Carlotti, M., von Clarmann, T., Delbouille, L., Dudhia,
681   A., Ehhalt, D., Endemann, M., Flaud, J. M., Gessner, R., Kleinert, A., Koopman, R., Langen,
682   J., Lopez-Puertas, M., Mosner, P., Nett, H., Oelhaf, H., Perron, G., Remedios, J., Ridolfi, M.,
683   Stiller, G., and Zander, R.: MIPAS: an instrument for atmospheric and climate research,
684   Atmos. Chem. Phys., 8, 2151-2188, doi:10.5194/acp-8-2151-2008, 2008.

685   Flesch, T. K., Wilson, J. D., Harper, L. A., Todd, R. W., and Cole, N. A.: Determining ammonia
686   emissions from a cattle feedlot with an inverse dispersion technique, Agric. For. Meteorol.,
687   144, 139-155, ISSN: 0168-1923, doi: 10.1016/j.agrformet.2007.02.006, 2007.

688   Follette-Cook, M. B., et al.: Spatial and temporal variability of trace gas columns derived from
689   WRF/Chem regional model output: Planning for geostationary observations of atmospheric
690   composition, Atmos. Env., 118, 28-44, ISSN: 1352-2310,
691   doi:10.1016/j.atmosenv.2015.07.024, 2015.

692   Franco, B., et al.: Retrievals of formaldehyde from ground-based FTIR and MAX-DOAS
693   observations at the Jungfraujoch station and comparisons with GEOS-Chem and IMAGES
694   model simulations, Atmos. Meas. Tech., 8, 1733-1756, doi:10.5194/amt-8-1733-2015, 2015.

695   Fried, A., et al.: Photochemistry of formaldehyde during the 1993 Tropospheric OH
696   Photochemistry Experiment, J. Geophys. Res., 102, 6283-6296, doi:10.1029/96JD03249,
697   1997.

698   Glatthor, N., von Clarmann, T., Stiller, G. P., Funke, B., Koukouli, M. E., Fischer, H.,
699   Grabowski, U., Höpfner, M., Kellmann, S., and Linden, A.: Large-scale upper tropospheric
700   pollution observed by MIPAS HCN and C_2H_6 global distributions, Atmos. Chem. Phys., 9,
701   9619-9634, doi:10.5194/acp-9-9619-2009, 2009.

702   Harris, D., Foufoula-Georgiou, E., Droegemeier, K. K., and Levit, J. J.: Multiscale statistical
703   properties of a high resolution precipitation forecast, J. Hydrometeorol, 2, 406-418, 2001.

704   Harrison, J. J., Nicholas D.C. Allen, Peter F. Bernath, Infrared absorption cross sections for
705   ethane (C2H6) in the 3 μm region, J. Quant. Spectrosc. Radiat. Transfer, 111(3), 357-363,
706   ISSN 0022-4073, doi.org/10.1016/j.jqsrt.2009.09.010, 2010.

707   Hase, F., Blumenstock, T., and Paton-Walsh, C.: Analysis of the instrumental line shape of high-
708   resolution Fourier transform IR spectrometers with gas cell measurements and new retrieval
709   software, Appl. Opt., 38, 3417-3422, doi:10.1364/AO.38.003417, 1999.

710   Hase, F., Hannigan, J. W., Coffey, M. T., Goldman, A., Höpfner, M., Jones, N. B., Rinsland, C.
711   P., and Wood, S. W.: Intercomparison of retrieval codes used for the analysis of high-
712   resolution, ground-based FTIR measurements, J. Quant. Spectrosc. Radiat. Transfer, 87(1),
713   25-52, doi:10.1016/j.jqsrt.2003.12.008, 2004.

714   Hase, F., Frey, M., Blumenstock, T., Groß, J., Kiel, M., Kohlhepp, R., Mengistu Tsidu, G.,
715   Schäfer, K., Sha, M. K., and Orphal, J.: Application of portable FTIR spectrometers for
716   detecting greenhouse gas emissions of the major city Berlin, Atmos. Meas. Tech., 8, 3059-
717   3068, doi:10.5194/amt-8-3059-2015, 2015.

718   Hristov, A. N., Hanigan, M., Cole, A., Todd, R., McAllister, T. A., Ndegwa, P. M., and Rotz, A.:
719   Review: Ammonia emissions from dairy farms and beef feedlots, Can. J. Anim. Sci., 91(1), 1-
720   35, doi:10.4141/CJAS10034, 2011

721   Hutchinson, G. L., Mosier, A. R., and Andre, C. E.: Ammonia and Amine Emissions from a
722   Large   Cattle   Feedlot,   J.   Environ.   Qual.,   11,   288-293,   doi:
723   10.2134/jeq1982.00472425001100020028x, 1982.

724   Ibrahim, O., Shaiganfar, R., Sinreich, R., Stein, T., Platt, U., and Wagner, T.: Car MAX-DOAS
725   measurements around entire cities: quantification of NO_x emissions from the cities of
726   Mannheim and Ludwigshafen (Germany), Atmos. Meas. Tech., 3, 709-721, doi:10.5194/amt-
727   3-709-2010, 2010.

Atmospheric
Measurement
Techniques
Discussions

Open Access

EGU

728　IUPAC, Compendium of Chemical Terminology, 2nd ed. (the "Gold Book"), Compiled by

729　　McNaught, A. D., and Wilkinson, A., Blackwell Scientific Publications, Oxford,

730　　doi:10.1351/goldbook, 1997.

731　Jaeglé, L., Steinberger, L., Martin, R. V., and Chance, K.: Global partitioning of NO_x sources

732　　using satellite observations: Relative roles of fossil fuel combustion, biomass burning and soil

733　　emission, Faraday Discuss., 130, 407-423, doi:10.1039/b502128f, 2005.

734　Jones, E.: EPA Updates Emission Standards for Petroleum Refineries/First-ever fenceline

735　　monitoring　　　requirements　　　will　　　protect　　　nearby　　　communities,

736　　https://yosemite.epa.gov/opa/admpress.nsf/0/D12EDC1C383ADF0385257ECF005B96B6,

737　　2015.

738　Kissinger, W. F., Koelsch, R. K., Erickson, G. E., and Klopfenstein, T. J.: Characteristics of

739　　manure harvested from beef cattle feedlots, Appl. Eng. Agric., 23(3), 357-365, 2007.

740　Kleiner, I., Tarrago, G., Cottaz, C., Sagui, L., Brown, L. R., Poynter, R. L., Pickett, H. M., Chen,

741　　P., Pearson, J. C., Sams, R. L., Blake, G. A., Matsuura, S., Nemtchinov, V., Varanasi, P.,

742　　Fusina, L., and Di Lonardo, G.: NH3 and PH3 line parameters: the 2000 HITRAN update and

743　　new results, J. Quant. Spectrosc. Radiat. Transfer, 82(1–4), 293-312, ISSN 0022-4073,

744　　doi:10.1016/S0022-4073(03)00159-6, 2003.

745　Lei, W., Zavala, M., de Foy, B., Volkamer, R., Molina, M. J., and Molina, L. T.: Impact of

746　　primary formaldehyde on air pollution in the Mexico City Metropolitan Area, Atmos. Chem.

747　　Phys., 9, 2607-2618, doi:10.5194/acp-9-2607-2009, 2009.

748　Leytem, A. B., Dungan, R. S., Bjorneberg, D. L., and Koehn, A. C.: Greenhouse Gas and

749　　Ammonia Emissions from an Open-Freestall Dairy in Southern Idaho, J. Environ. Qual., 42,

750　　10-20, doi:10.2134/jeq2012.0106, 2013.

751　Long, G. L., and Winefordner, J. D.: Limit of detection, A closer look at the IUPAC definition,

752　　Anal. Chem., 55(7), 712A-724A, doi:10.1021/ac00258a001, 1983.

753　Lou, Y., Zhang, Q., Wang, H., and Wang, Y.: Catalytic oxidation of ethylene and ethane to

754　　formaldehyde　by　oxygen,　J.　Catal.,　250,　365-368,　ISSN:　0021-9517,

755　　doi:10.1016/j.jcat.2007.06.015, 2007.

Atmospheric
Measurement
Techniques
Discussions

756   Mellqvist, J., Samuelsson, J., Johansson, J., Rivera, C., Lefer, B., Alvarez, S., and Jolly, J.:
757   Measurements of industrial emissions of alkenes in Texas using the solar occultation flux
758   method, J. Geophys. Res., 115, D00F17, doi:10.1029/2008JD011682, 2010.

759   Miller, D. J., Sun, K., Tao, L., Pan, D., Zondlo, M. A., Nowak, J. B., Liu, Z., Diskin, G., Sachse,
760   G., Beyersdorf, A., Ferrare, R., and Scarino, A. J.: Ammonia and methane dairy emission
761   plumes in the San Joaquin Valley of California from individual feedlot to regional scales, J.
762   Geophys. Res. Atmos., 120, 9718-9738, doi:10.1002/2015JD023241, 2015.

763   Mukhtar, S., Mutlu, A., Capareda, S. C., and Parneli, C. B.: Seasonal and Spatial Variations of
764   Ammonia Emissions from an Open-Lot Dairy Operation, J. Air Waste Manag. Assoc., 58(3),
765   369-376, doi:10.3155/1047-3289.58.3.369, 2008.

766   Nussbaumer, E., and Hannigan, J.: Infrared Working Group Retrieval Code, SFIT,
767   https://wiki.ucar.edu/display/sfit4/Infrared+Working+Group+Retrieval+Code,+SFIT, 2014.

768   Ortega, I., Koenig, T., Sinreich, R., Thomson, D., and Volkamer, R.: The CU 2-D MAX-DOAS
769   instrument – Part 1: 3-D Retrieval of NO2 and azimuth dependent OVOC ratios, Atmos.
770   Meas. Tech., 8, 2371-2395, doi:10.5194/amt-8-2371-2015, 2015.

771   Parrish, D. D., and Fehsenfeld, F. C.: Methods for gas-phase measurements of ozone, ozone
772   precursors and aerosol precursors, Atmos. Env., 34(12–14), 1921-1957, ISSN 1352-2310,
773   doi:10.1016/S1352-2310(99)00454-9, 2000.

774   Pierce, G.: Air Quality Reports, Colorado Air Quality Department of Public Health and
775   Environment, http://www.colorado.gov/airquality/report.aspx, 2016.

776   Raga, G. B., Baumgardner, D., Castro, T., Martinez-Arroyo, A., and Navarro-Gonzalez, R.:
777   Mexico City air quality: a qualitative review of gas and aerosol measurements (1960-2000),
778   Atmos. Env., 35(23), 4041-4058, ISSN: 1352-2310, doi:10.1016/S1352-2310(01)00157-1,
779   2001.

780   Ramanathan, V., and Feng, Y.: Air pollution, greenhouse gases and climate change: Global and
781   regional   perspectives,   Atmos.   Env.,   43(1),   37-50,   ISSN: 1352-2310,
782   doi:10.1016/j.atmosenv.2008.09.063, 2009.

Atmospheric
Measurement
Techniques
Discussions

Open Access

EGU

783 Rinsland, C. P., Dufour, G., Boone, C. D., Bernath, P. F., and Chiou, L.: Atmospheric Chemistry
784   Experiment (ACE) measurements of elevated Southern Hemisphere upper tropospheric CO,
785   C_2H_6, HCN, and C_2H_2 mixing ratios from biomass burning emissions and long-range
786   transport, Geophys. Res. Lett., 32, L20803, doi:10.1029/2005GL024214, 2005.

787 Rothman, L. S., et al.: The HITRAN 2008 molecular spectroscopic database, J. Quant. Spectrosc.
788   Radiat. Transfer, 110, 9(10), 533-572, doi:10.1016/j.jqsrt.2009.02.013, 2009.

789 Sander, S. P., Friedl, R. R., Golden, D. M., Kurylo, M. J., Moortgat, G. K., Keller-Rudek, H.,
790   Wine, P. H., Ravishankara, A. R., Kolb, C. E., Molina, M. J., Finlayson-Pitts, B. J., Huie, R.
791   E., and Orkin, V. L.: Chemical Kinetics and Photochemical Data for Use in Atmospheric
792   Studies, Evaluation Number 15, JPL Publication 06-2, 2006.

793 Schrader, B.: Infrared and Raman Spectroscopy, VCH, Weinheim, Germany, 1995.

794 Shephard, M. W., Cady-Peireira, K. E., Luo, M., Henze, D. K., Pinder, R. W., Walker, J. T.,
795   Rinsland, C. P., Bash, J. O., Zhu, L., Payne, V. H., and Clarisse, L.: TES ammonia retrieval
796   strategy and global observations of the spatial and seasonal variability of ammonia, Atmos.
797   Chem. Phys., 11, 10743–10763, doi:10.5194/acp-11-10743-2011, 2011.

798 Stocker, T. F., D. Qin, G.-K. Plattner, M. Tignor, S.K. Allen, J. Boschung, A. Nauels, Y. Xia, V.
799   Bex, and P.M. Midgley, editors. IPCC, 2013: Climate Change 2013: The Physical Science
800   Basis. Contribution of Working Group I to the Fifth Assessment Report of the
801   Intergovernmental Panel on Climate Change. Cambridge University Press, Cambridge,
802   United Kingdom and New York, NY, USA, 2013.

803 Todd, R. W., Cole, N. A., Clark, R. N., Flesch, T. K., Harper, L. A., and Baek, B. H.: Ammonia
804   emissions from a beef cattle feedyard on the southern High Plains, J. Atmos. Env., 42(28),
805   6797-6805, doi:10.1016/j.atmosenv.2008.05.013, 2008.

806 Van Damme, M., Clarisse, L., Heald, C. L., Hurtmans, D., Ngadi, Y., Clerbaux, C., Dolman, A.
807   J., Erisman, J. W., and Coheur, P. F.: Global distributions, time series and error
808   characterization of atmospheric ammonia (NH_3) from IASI satellite observations, Atmos.
809   Chem. Phys., 14, 2905-2922, doi:10.5194/acp-14-2905-2014, 2014.

810 Van Roozendael, M., and Fayt, C.: WinDOAS 2.1, 2001.

Atmospheric
Measurement
Techniques
Open Access
Discussions
EGU

811   Walker, J. T., Dave R Whitall, Wayne Robarge, Hans W. Paerl, Ambient ammonia and
812   ammonium aerosol across a region of variable ammonia emission density, Atmospheric
813   Environment, 38(9), 1235-1246, ISSN 1352-2310, doi:10.1016/j.atmosenv.2003.11.027,
814   2004.

815   Xiao, Y., Logan, J. A., Jacob, D. J., Hudman, R. C., Yantosca, R., and Blake, D. R.: Global
816   budget of ethane and regional constraints on U.S. sources, J. Geophys. Res., 113, D21306,
817   doi:10.1029/2007JD009415, 2008.

818   Zhang, R., Suh, I., Zhao, J., Zhang, D., Fortner, E. C., Tie, X., Molina, L. T., and Molina, M. J.:
819   Atmospheric New Particle Formation Enhanced by Organic Acids, Science, 304(5676), 1487-
820   1490, doi:10.1126/science.1095139, 2004.

821   Zhang, Q., et al.: Ubiquity and dominance of oxygenated species in organic aerosols in
822   anthropogenically-influenced Northern Hemisphere midlatitudes, Geophys. Res. Lett., 34,
823   L13801, doi:10.1029/2007GL029979, 2007.

824   Zörner, J., Penning de Vries, M. J. M., Beirle, S., Sihler, H., Veres, P. R., Williams, J., and
825   Wagner, T.: Multi-satellite sensor study on precipitation-induced emission pulses of NO_x
826   from soils in semi-arid ecosystems, Atmos. Chem. Phys. Discuss., doi:10.5194/acp-2016-93,
827   2016.

828

Atmospheric
Measurement
Techniques
Open Access
Discussions
EGU

829   Table 1. Specifications of the CU mobile SOF instrument.

Characteristic	Mid-IR		UV-Vis
	Channel 1	Channel 2	Channel 3
Spectrometer	Michelson interferometer		Grating spectrometer
	EM27		QE65000
Spectral resolution	0.5 cm^{-1}		~0.55 nm
Detector	MCT	InSb	CCD[3]
Spectral range	700 – 1850 cm^{-1}	1850 – 5000 cm^{-1}	390 – 520 nm
Dimensions[1]	860 mm x 520 mm x 600 mm		
Weight[1]	~45 kg		
Power requirement[2]	115V AC, 380 W		

830   [1] includes the solar tracker, spectrometers and base plate.

831   [2] includes the solar tracker, spectrometers, laptops for data acquisition and control electronics.

832   [3] charge-coupled device

833

Atmospheric
Measurement
Techniques

Open Access

EGU

Discussions

834   Table 2: Spectral fit windows used in the retrievals.

Target species	Interfering species	Wavenumber range
NH_3	O_3, H_2O, CO_2, C_2H_4	$950 - 980$ cm^{-1}
C_2H_6	CH_3Cl, H_2O, HDO, CH_4	$2970 - 3000$ cm^{-1}
NO_2	O_3, H_2O, O_4, $C_2H_2O_2$, CLD[1]	$434 - 460$ nm

835   [1] Center to limb darkening (CLD)

836   Table 3: Overview of SFIT4 a-priori values.

species	a-priori [molec/cm^2]	a-priori error [%]
C_2H_6	1.18×10^{16}	10,000
NH_3	2.23×10^{13}	10,000
CH_3Cl	8.88×10^{15}	1000
H_2O	3.78×10^{22}	50
HDO	1.43×10^{23}	50
CH_4	3.12×10^{19}	100
O_3	8.44×10^{18}	1
C_2H_4	3.75×10^{14}	10
CO_2	6.65×10^{21}	10

837

Atmospheric
Measurement
Techniques

Open Access

Discussions

EGU

838   Table 4: Results of the FTS quality assurance.

	channel 1/ NH_3	channel 2/ C_2H_6
Precision[1] [10^{16} molec/cm^2]	0.01	0.01
Accuracy[2] [10^{16} molec/cm^2]	0.07	0.10
LOD [10^{16} molec/cm^2]	**0.10**	**0.13**
Total error [%]	**4.4**	**6.7**
• OPD effect[3] [%]	0.5	0.0
• Cross section uncertainty [%]	2.0[4]	4.0[5]
• Fit uncertainty [%]	1.9	2.7

839   [1] Calculated as the mean during periods in which the atmosphere remained constant

840   [2] Calculated as the difference between the CU mobile lab FTS and the NCAR high resolution

841   FTS

842   [3] Calculated for a median VCD of 4.32 x 10^{16} molec/cm^2 for NH_3 and 3.49 x 10^{16} molec/cm^2 for

843   C_2H_6 as measured during RD10 and RD11

844   [4] source: Kleiner et al. (2003)

845   [5] source: Harrison et al. (2010)

846

Atmospheric
Measurement
Techniques
Open Access
Discussions
EGU

847   Table 5: C_2H_6 and NH_3 flux estimates from 12 August (RD10) and the case study on 13 August

848   2014 (RD11) and NH_3 comparison to literature. The uncertainty on the fluxes is assuming the

849   model wind has an uncertainty of 30 %.

Site	1	2	4
Size [km x km]	1.6 x 1.6	1.6 x 1.6	1.6 x 1.6
Source Type	Dairy	Beef	Dairy
Maximum Count[1]	unknown	54,044	7,450
NH_3 Flux [kg/hr] – RD10	128 ± 38	625 ± 188	85 ± 26
NH_3 Flux [kg/hr] – RD11	89 ± 27	673 ± 202	NN[2]
NO_2 Flux [kg/hr] – RD10	NN[2]	18 ± 5	1.3 ± 0.4
NO_2 Flux [kg/hr] – RD11	NN[2]	11 ± 3	-2.5 ± 0.8[3]
C_2H_6 Flux [kg/hr] – RD10	37 ± 11[3]	NN[2]	NN[2]
C_2H_6 Flux [kg/hr] – RD11	90 ± 27[3]	NN[2]	NN[2]

850   [1] source: CDPHE (Colorado Department of Public Health and Environment): CAFO locations

851   and maximum capacities for FRAPPE (Daniel Bon, 2016, personal communication).

852   [2] NN = no number; significant influence from upwind sources precludes quantification.

853   [3] Influence from upwind sources is non-negligible.

854   Table 6: Comparison of ammonia emission rates from cattle with literature values.

Location	Cattle	Number of cattle	Method	Ambient condition	NH$_3$ flux [g/hr/head]	Reference
Colorado	Beef	54,044	Mobile SOF	August, 28 ± 3 °C	12.0 ± 2.8	This work
	Dairy	7,450		August, 32 ± 2 °C	11.4 ± 3.5	
	Pooled	--		August, 30 ± 5 °C	11.8 ± 2.1	
Texas	Beef	50,000	Open-path laser	Summer/Spring	6.25	Flesch et al. [2007]
Nebraska	Beef	6,366	--	Summer/Fall	6.79	Kissinger et al. [2007]
				Winter/Spring	4.96	
Victoria, Australia	Beef	17,700	Closed-path gas analyzer	August, daytime	5.21	Denmead et al. [2008]
Queensland, Australia	Beef	16,800		August/September, daytime	3.12	
Texas	Beef	44,651	Acid gas washing samplers mounted on a tower	July/August	5.25 ± 0.33	Todd et al. [2008]
				January/February	2.81 ± 0.97	
Texas	Dairy	2,000	Mobile chemiluminescence analyzer	July, 26 ± 1 °C	1.32 ± 0.81	Mukhtar et al. [2008]
				December, 6 ± 0.4 °C	0.71 ± 0.42	
Idaho	Dairy	700	Open-path FTS (OP/FTS)	January, -8 – 2 °C	1.66	Bjorneberg et al. [2009]
				March, -1 – 14 °C	10.4	
				June, 8 – 43 °C	7.92	
				September, 5 – 23 °C	6.25	
Idaho	Dairy	10,000	Photoacoustic gas monitors, OP/FTS	June/July/August, 16 – 24 °C	4.62 ± 0.83	Leytem et al. [2013]
				December/January, -8 – -5 °C	0.54 ± 0.11	
California	Dairy	--	Mobile wavelength modulation absorption spectroscopy	January, 9 – 20 °C	1.87 ± 0.40	Miller et al. [2015]

855

856   Table 7: Variability length scale of NH_3, NO_2, and C_2H_6.

	$L_V(50\%)$ [km][a]	$L_V(90\%)$ [km][b]	$L_V(LOD)$ [km][c]
NH_3	1.625	5.625	0.075
NO_2	1.825	5.525	1.725
C_2H_6	1.225	6.175	0.425

857   [a] Length at which 50 % of the variability with respect to the median VCD occurs.

858   [b] Length at which 90 % of the variability with respect to the median VCD occurs.

859   [c] Length scale at which the VCD difference is equal to the value of the LOD.

860

Atmospheric
Measurement
Techniques
Discussions

Open Access

EGU
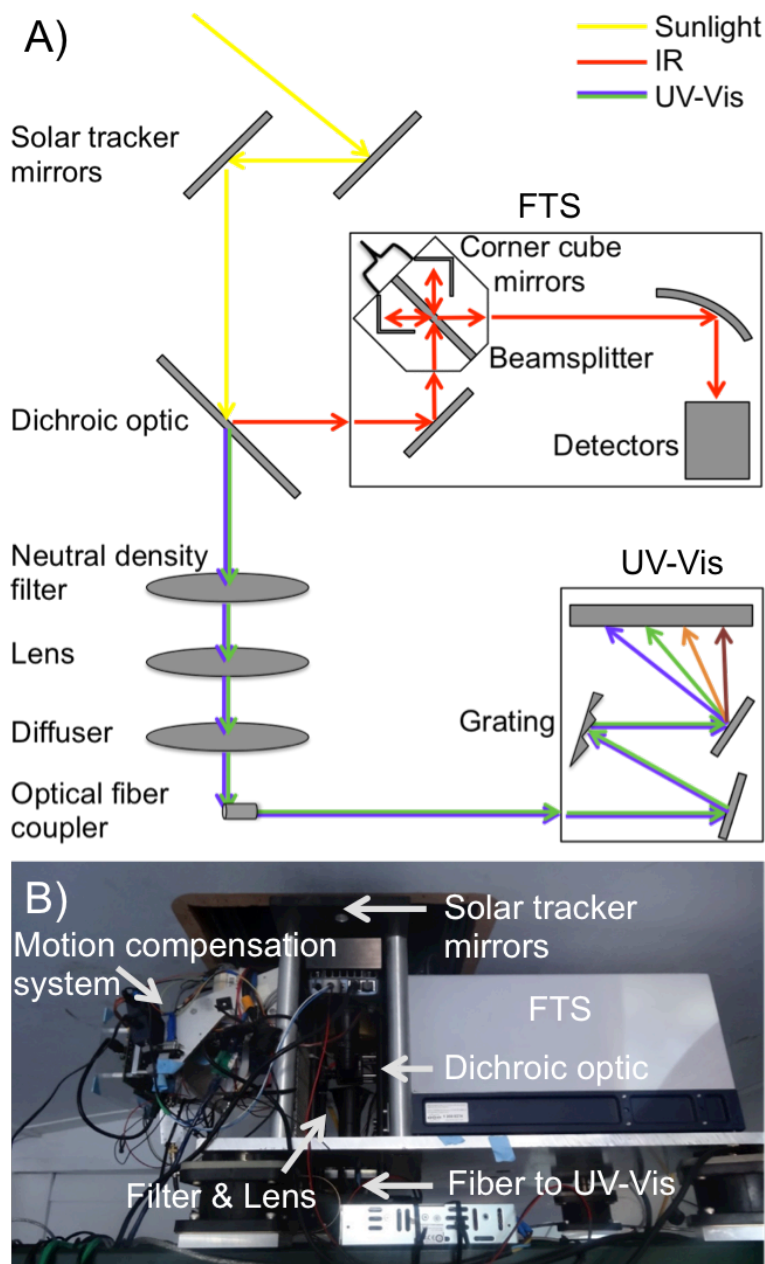
861

862   Figure 1. A) Conceptual sketch of the mobile SOF instrument components, B) Picture of the

863   instrument installed inside the trailer.

864

Atmospheric
Measurement
Techniques
Discussions
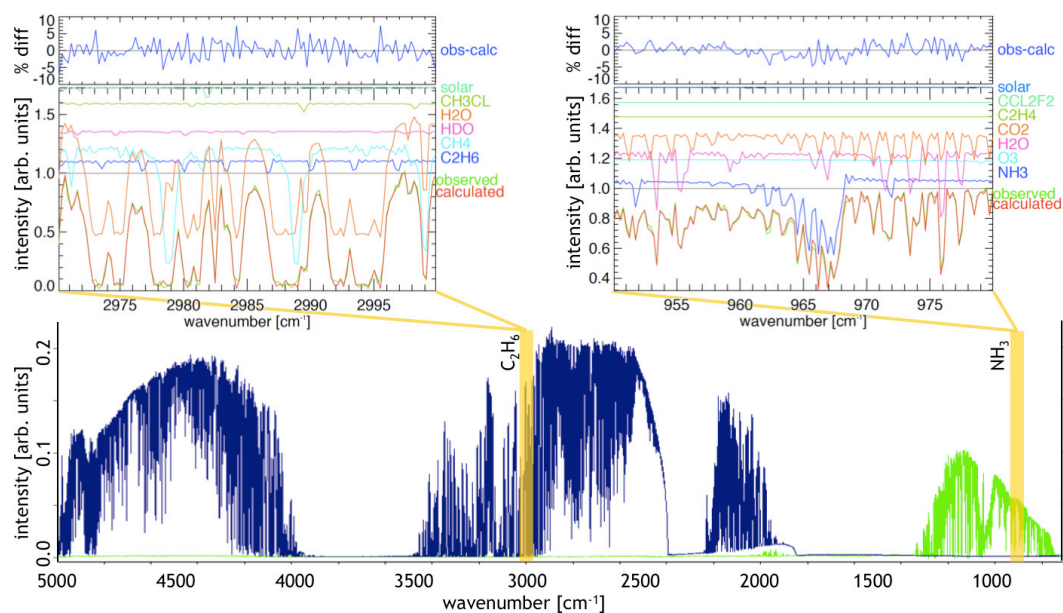
865

866

867   Figure 2. Solar spectrum measured by the InSb (blue) and MCT (green) detectors. Yellow bars

868   indicate the spectral intervals used for the retrieval of C_2H_6 and NH_3. Spectral proof of C_2H_6 (top

869   left) and NH_3 (top right). The C_2H_6 column was 7.13×10^{16} molecules/cm^2 (%rms=2.7), the NH_3

870   column was 40.2×10^{16} molecules/cm^2 (%rms=1.9) for the retrievals shown.

871
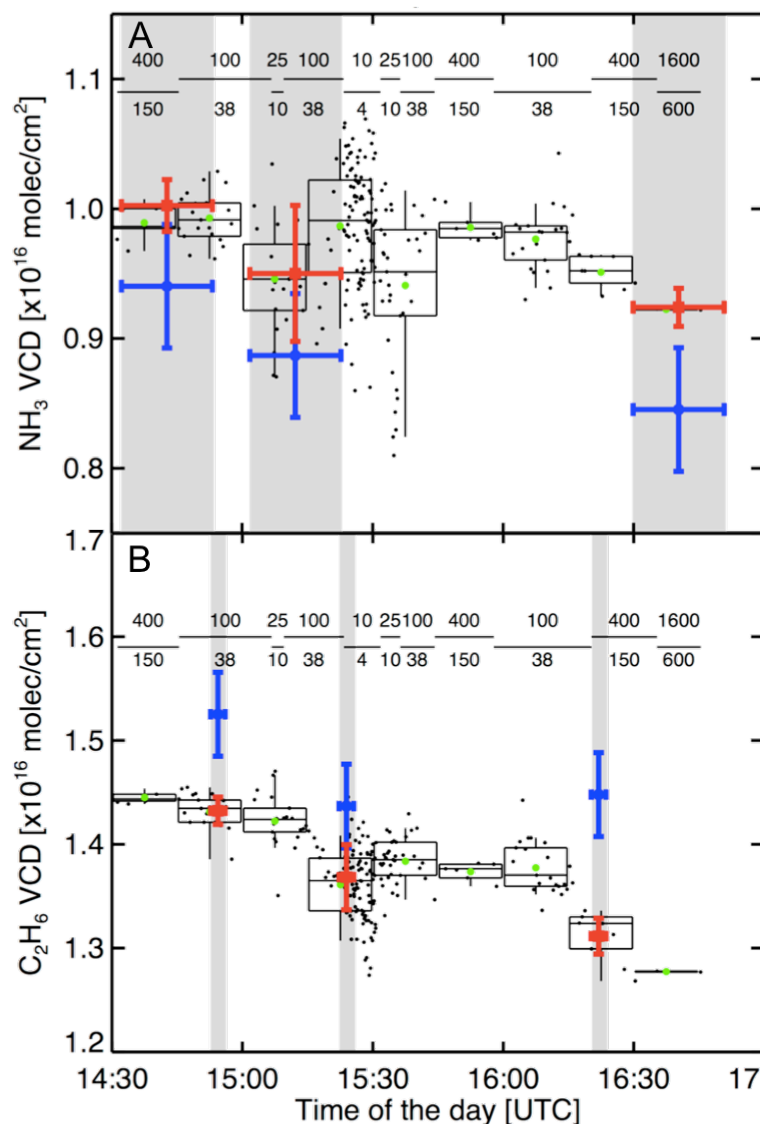
Figure 3. Assessment of CU mobile SOF accuracy at NCAR, Boulder, CO: A) NH_3, and B) C_2H_6; (blue) measurements of the HR-NCAR-FTS; (black) individual mobile SOF measurements (variable integration time); (red) mobile SOF data averaged over the time period of the NCAR measurements (indicated in grey); (green) 15min averages of mobile SOF data. The dashes indicate during which time period the individual mobile SOF measurements were taken. Numbers above the dashes indicate the internally co-added scan number, numbers below indicate the integration time of each stored spectrum in seconds.

40

Atmospheric
Measurement
Techniques
Discussions

879
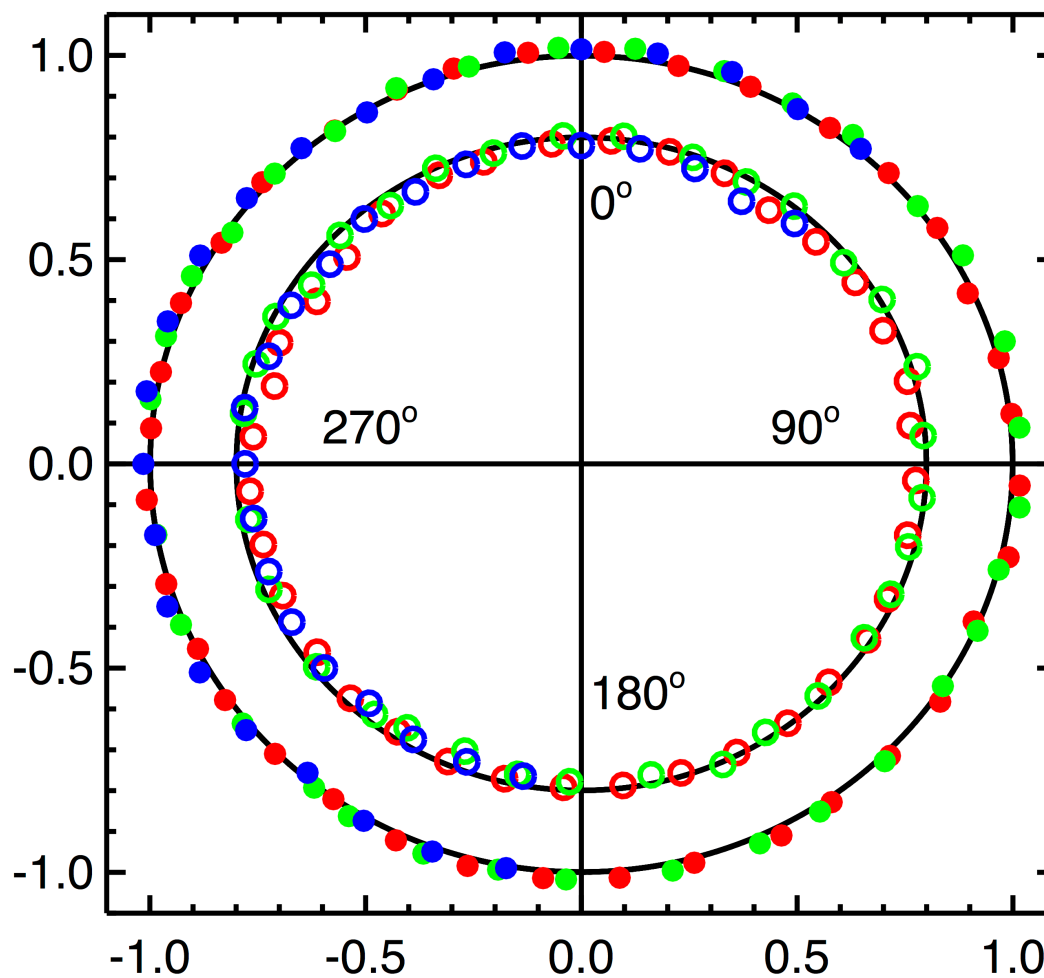
Figure 4. Angle dependence of the Instrument Line Shape (ILS) modulation efficiency at maximum OPD. MCT detector: open circles. InSb detector: filled circles. Green, red, and blue measured at an elevation angle of 5°, 45°, and 65°, respectively. The black unit circles represent an ideal ILS. See text for details.

Atmospheric
Measurement
Techniques
Discussions

Open Access

EGU

884
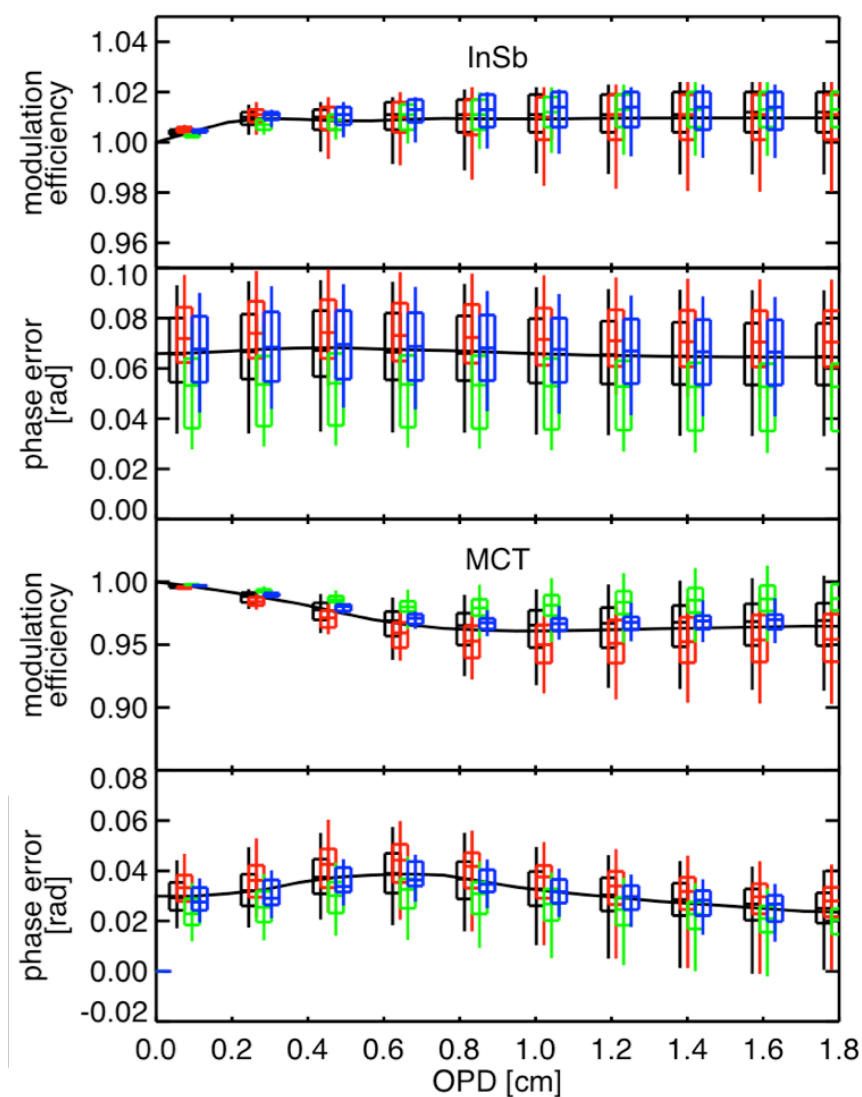
Figure 5. Instrument Line Shape (ILS) modulation efficiency and phase error as a function of optical path difference (OPD). Top panels: InSb detector. Bottom panels: MCT detector. Boxes mark 25th and 75th percentiles, the line inside the box marks the median. Lines outside the boxes indicate 5th and 95th percentile. Green, red, and blue represent averages over an elevation angle of 5°, 45°, 65°, respectively. Black is the average over all data. The different colored whiskers are off-set with respect to the OPD for visualization; green whiskers are located at the exact OPD.

891
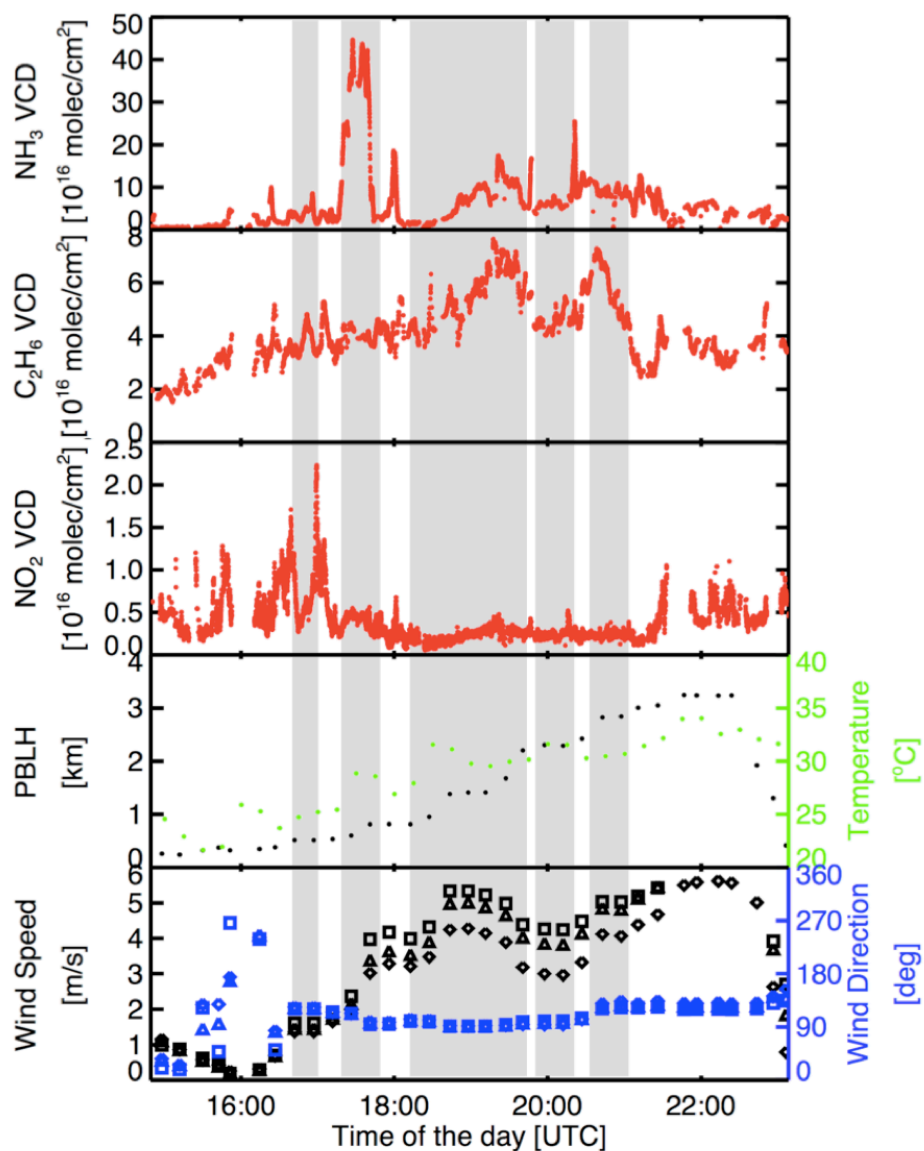
42

Atmospheric
Measurement
Techniques
Discussions
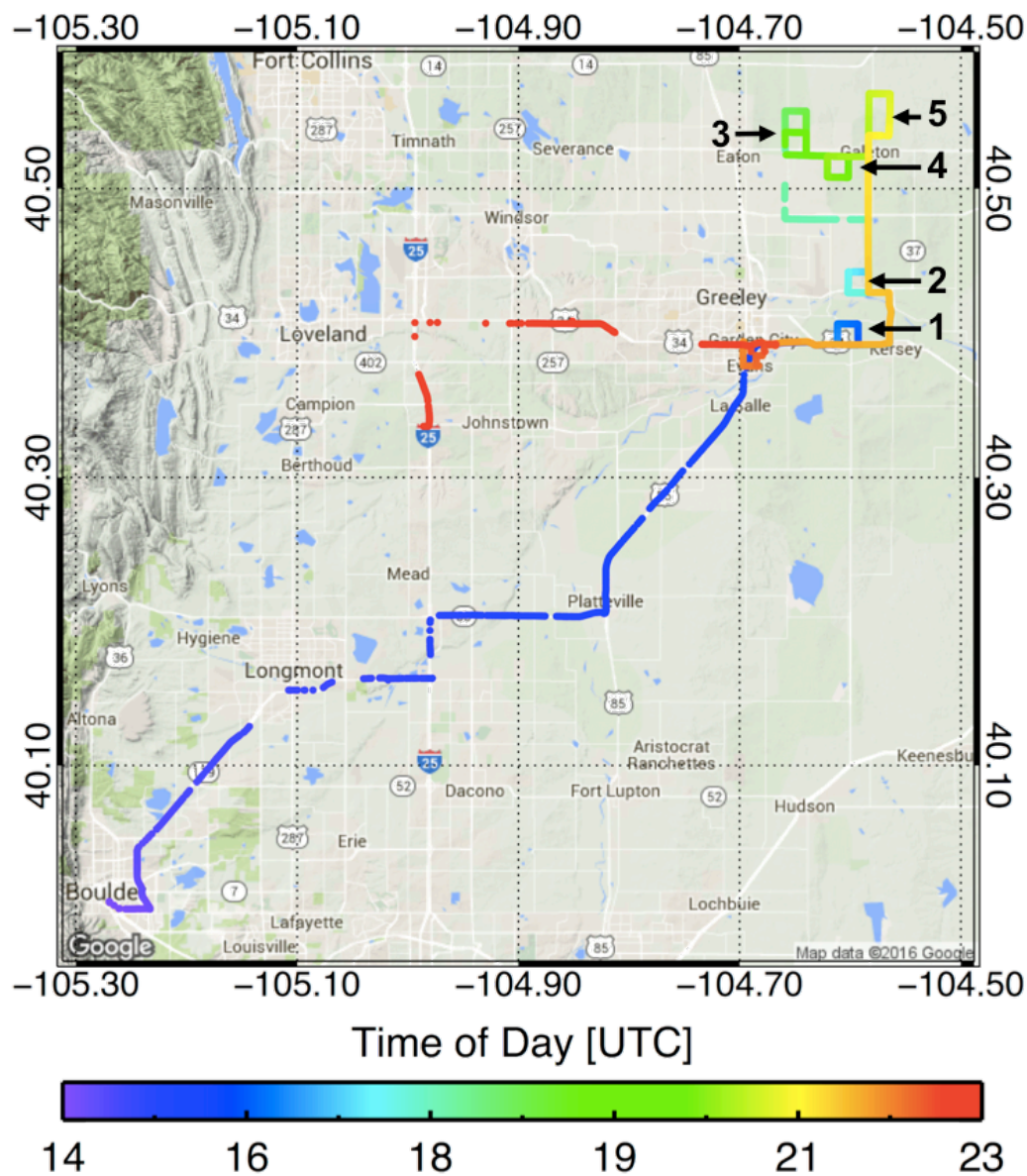
892

893   Figure 6. Research drive track of RD11 to investigate agricultural sources near Greeley, CO.

894   Sites: (1, 4, 5) dairy farms; (2) beef farm; (3) sheep farm.

895

896   Figure 7. Timeseries of the VCDs measured for A) NH$_3$, B) C$_2$H$_6$, C) NO$_2$, during RD11. D)

897   PBLH and temperature, E) model wind; (diamonds) model wind averaged over approximately

898   10-50 m above ground level, (triangles) over half PBLH, (squares) over the full PBLH. Shaded

899   areas indicate times at each site (numbers correspond to those in Fig. 6).

44

Atmospheric
Measurement
Techniques

Open Access

Discussions

900
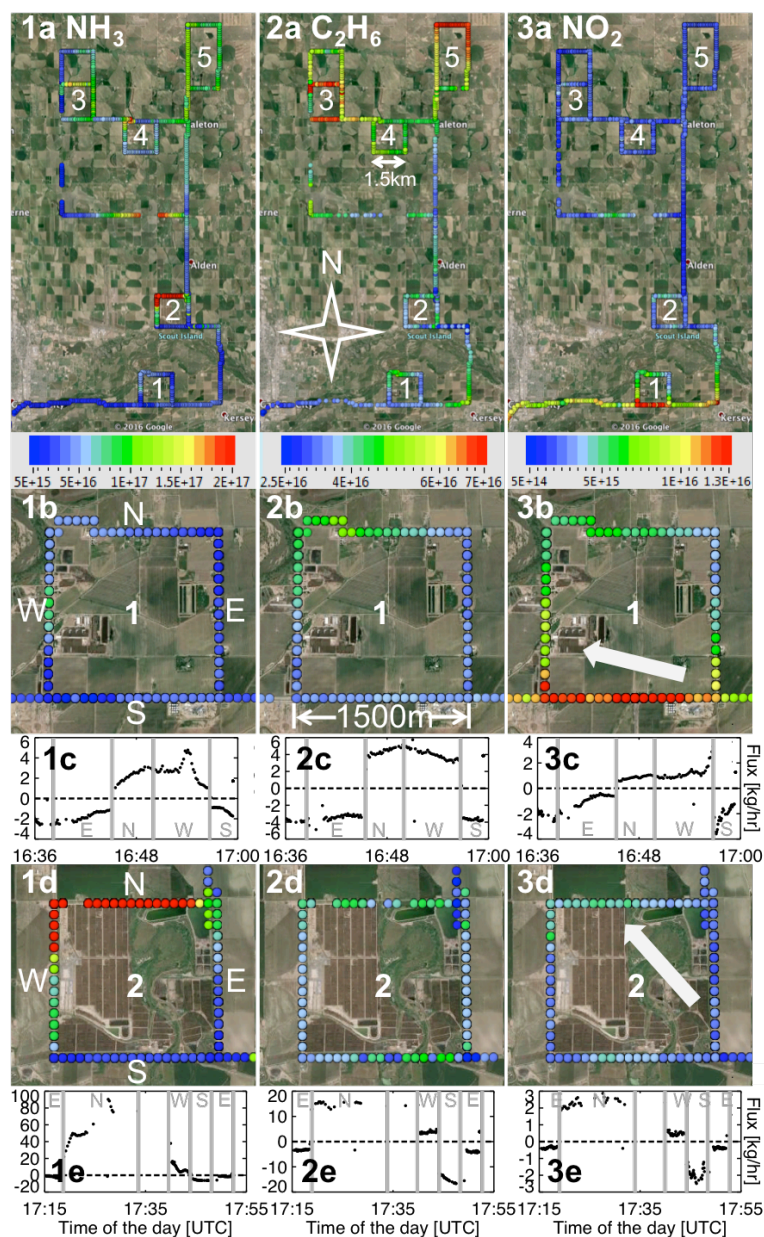
Figure 8. Zoom of the area east of Greeley, CO with the RD11 drive track color coded by the
VCD of (left column, 1) NH_3, (middle, 2) C_2H_6, and (right, 3) NO_2. Row (a) shows the 5 sites of
interest, (b) site 1, (d) site 2 from Fig. 6. Rows (c) and (e) show a timeseries of the flux,
calculated using Eq. 1; the arrows in 3b and 3d indicate the mean wind direction at each site.
(Background image from Google Earth 2016)

906
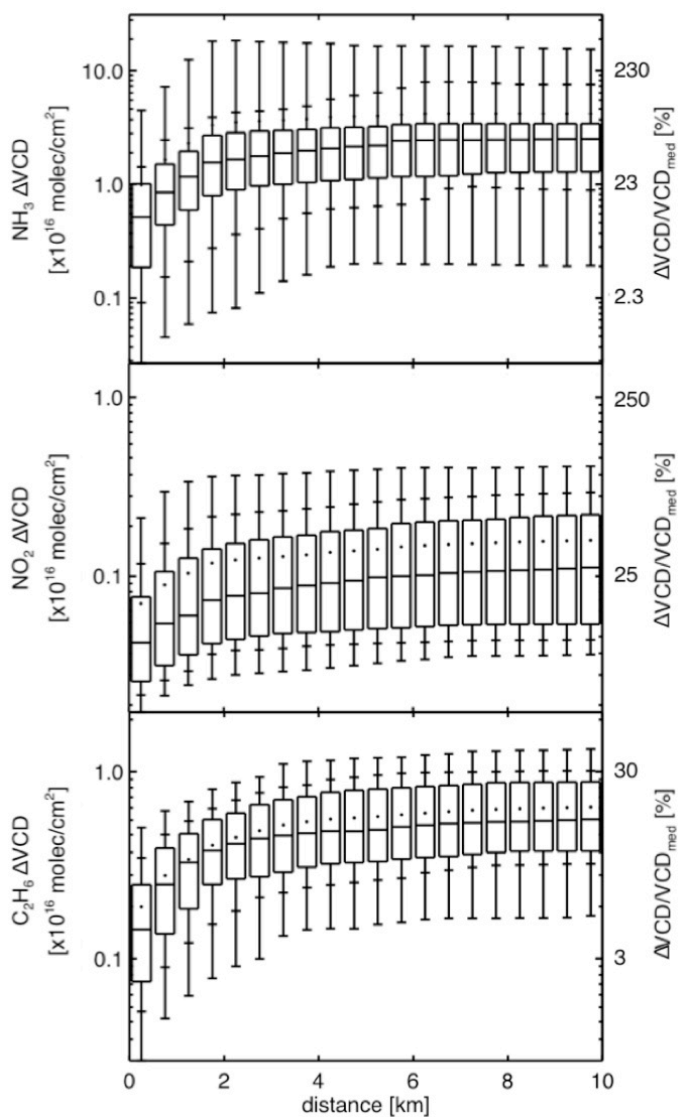
Figure 9. Structure functions of (A) NH_3, (B) C_2H_6, and (C) NO_2 using data from RD11 with a time constraint of 30 min for the timeperiod of the 5 sites. The binwidth is 500 m. Boxes mark 25th and 75th percentiles, the dot indicates the mean, the line inside the box marks the median. Dashes below and above the boxes indicate 5th, 15th, 85th, and 95th percentile.